Nanoscale

ROYAL SOCIETY OF CHEMISTRY

PAPER

View Article Online
View Journal | View Issue

Cite this: *Nanoscale*, 2024, **16**, 1770

Nitric oxide releasing novel amino acid-derived polymeric nanotherapeutic with anti-inflammatory properties for rapid wound tissue regeneration†

Prem Shankar Gupta, ‡[a] Kirti Wasnik, ‡[a] Sukanya Patra,[a] Divya Pareek, [a] Gurmeet Singh, [a] Desh Deepak Yadav, [a] Somedutta Maity [b] and Pradip Paik *[a]

Endogenous gasotransmitter nitric oxide (NO) is a central signalling molecule that modulates wound healing by maintaining homeostasis, collagen formation, wound contraction, anti-microbial action and accelerating tissue regeneration. The optimum delivery of NO using nanoparticles (NPs) is clinically challenging; hence, it is drawing significant attention in wound healing. Herein, a novel polymeric nanoplatform loaded with sodium nitroprusside (SP) NPs was prepared and used for wound healing to obtain the sustained release of NO in therapeutic quantities. SP NPs-induced excellent proliferation (~300%) of mouse fibroblast (L929) cells was observed. With an increase in the SP NPs dose at 200 μg mL^{-1} concentration, a 200% upsurge in proliferation was observed along with enhanced migration, and only 17.09 h were required to fill the 50% gap compared to 37.85 h required by the control group. Further, SP NPs showed an insignificant impact on the coagulation cascade, revealing safe wound-healing treatment when tested in isolated rat RBCs. Additionally, SP NPs exhibited excellent angiogenic activity at a 10 μg mL^{-1} dose. Moreover, the formulated SP nanoformulation is non-irritant, non-toxic, and does not produce any skin sensitivity reaction on the rat's skin. Further, an *in vivo* wound healing study revealed that within 11 days of treatment with SP nanoformulation, 99.2 ± 1.0% of the wound was closed, while in the control group, only 45.5 ± 3.8% was repaired. These results indicate that owing to sustained NO release, the SP NP and SP nanoformulations are paramount with enormous clinical potential for the regeneration of wound tissues.

Received 6th August 2023,
Accepted 14th December 2023

DOI: 10.1039/d3nr03923d

rsc.li/nanoscale

1. Introduction

Chronic wounds or hard-to-heal wounds negatively impact the quality of life, cause psychological stress and substantially increase the financial burden on patients.[1,2] According to epidemiology studies, in India, the prevalence rate of chronic wounds is estimated to be 4.5/1000 where major traumatic injuries are generally associated with diabetic cases. Various indigenous or exogenous factors impair wound healing mechanisms, leading to severe pathological sequelae and significant clinical challenges; therefore, it is considered a civilizational disease.[3]

Although many works on wound healing have been reported, a deeper understanding of the mechanism and implementation of more effective and cheaper treatment is an essential requirement. Further, wound healing in embryos and adults has some differences;[4] the significant differences observed are associated with the immune and inflammatory system and NO production, which is higher in the embryonic system than in an adult wound. It is reported that in the wound healing mechanism, endogenous gastro transmitter NO plays a crucial role in the regulation of overlapping phases of wound healing cascades.[5,6] Out of the many research reports available on different materials for therapeutic applications,[7] NO is mainly associated with inflammation, antibac-

[a]*School of Biomedical Engineering, Indian Institute of Technology (BHU), Varanasi, India. E-mail: paik.bme@iitbhu.ac.in*
[b]*School of Engineering Science and Technology, University of Hydrabad, Hydrabad, India*

†Electronic supplementary information (ESI) available: 1. Synthesis of NAG monomer, 2. fabrication of SP NPs, 3. characterization, 4. *in vivo* study, ethics and approval; Table S1: Formulation of SP nanoformulation, Table S2: Qualitative evaluation of SP nanoformulation, Table S3: Skin irritation evaluation; Scheme S1. Synthesis of NAG monomer; Fig. S1: Content uniformity test, Fig. S2: *In vitro* dissolution of SP nanoformulation, Fig. S3: ^{1}H NMR spectra of NAG monomer, Fig. S4: ^{13}C NMR spectra of NAG monomer, Fig. S5: FTIR spectra of NAG monomer, Fig. S6: PXRD pattern of NAG monomer, Fig. S7: Ninhydrin test, Fig. S8. Synthesis of PNAG NPs, Fig. S9. FTIR spectra of PNAG NPs, Fig. S10. Cytocompatibility PNAG NPs in L929 cells, Fig. S11. Histology of wound tissue. See DOI: https://doi.org/10.1039/d3nr03923d

‡These authors contributed equally.

terial activities, collagen production, cell proliferation, re-epithelialization, and angiogenesis, among others,[8] in adult wound healing. Therefore, if a controlled dose could be applied, NO-induced wound healing could be one of the most effective therapeutic options. Because NO can have several positive impacts on accelerated wound healing, its metabolites have been reported in correlation with the healing trajectory, suggesting the potential for recovery or aggravation.[9] It is reported that mice lacking inducible or endothelial NO synthase exhibit delayed wound repair and poor angiogenesis.[10–12] Impaired wound healing also results in blocking the knockdown of NOs or by the removal of NO by scavengers, and the emergence of chronic wounds is directly linked to turning down the supply of NO at the wounded sites.[13–15] However, the controlled release of NO content is crucial in wound healing. To increase the level of NO and consequently therapeutic efficiency, exogenous NO donors or stimulators can be used and administered either in the form of direct topical NO donor[16] or indirectly in the form of NO synthase (NOs) stimulator,[17] the transfer of the NOs gene, and the systemic delivery of the NOs substrate.[16] Earlier, silica NPs, gold NPs, liposomes, and dendrimers were used for the delivery of NO.[18,19] Polymeric nanoparticles can be used for NO delivery due to their advantages such as the precise and controlled release of NO, as discussed in our previous report.[20,21] Although several researches are focused on developing the stable and precise delivery of exogenous NO donors to increase the NO level at the wound site to accelerate the healing process,[22] the current challenges remain such as initial burst release poor biocompatibility and low loading capacity.[23] Therefore, developing the NO-releasing delivery system requires extreme care and expertise. Polymeric nanocarrier-based therapeutics of NO have proved promising as earlier from our proof of concept and it has been reported that NO delivery through these could enhance wound healing efficiency.[20] Further, due to fungi static, bacteriostatic, hemostatic, and collagen-forming properties of gelatin, chitosan, and antimicrobial peptides, they have some degree of wound-healing ability;[24,25] however, their therapeutic efficiency are unsatisfactory, and side effects including scar formation and infection, poor adhesive, hydrophobic nature, and uncontrolled polymerization were there in the long run, arising from the essential supply of new therapeutics, which will fulfil the current demand.[26] A rise in the toxicity with highly potent drugs always reduces their regular use in clinics, but with nanomedicine, there is always a hope that it will reduce the systemic damage and lower the toxicity by acting as nanoantidote and deliver compounds in a sustained and controlled manner with improved pharmaceutical stability.[27,28]

With the aim to overcome the above challenges and motivated with positive outcomes of nanomedicine, the present work is focused on the synthesis of an advanced biosafe material of poly-*N*-acryloyl glycine (PNAG) and formulated with a NO donor, sodium nitroprusside (SNP). Acryloyl glycine-based PNAG NPs are biocompatible, proven effective, and safe wound-healing materials with angiogenic and biodegradable capabilities and low cytotoxic effects. Due to the high NO content, quick metabolism, and ideal NO release property, SNP can be used as an NO-releasing drug. Clinically, SNP is frequently used to treat hypertensive emergencies and abrupt heart failure and is listed as one of the essential medicines by WHO.[29] NO-releasing polymeric nanoparticles could allow predictable and regulated NO delivery. The easiest and most efficient method to deliver NO to a cutaneous wound is the topical administration of NO-releasing or NO-generating biomaterials.[30] Therefore, to achieve optimum NO release, we designed an NO-releasing nanoformulation (SP nanoformulation) from NO-loaded PNAG NPs (SP NPs) and used it for wound healing. Herein, we have scrutinized the toleration of SP NPs against the mouse fibroblast (L929) cell lines and rat RBCs to show the effect on hemolysis. Further, we have studied the extent of proliferation and migration of L929 cells. The skin sensitization and irritation of SP nanoformulation have also been studied, and the levels of pro-inflammatory cytokines and chemokines during *in vivo* wound healing assessment have been investigated. Further, compared to previous NO-releasing therapeutics,[31] how these SP NPs and SP nanoformulation are advantageous such as stability, simplicity of application, and prolonged NO release have also been studied. Additionally, the cumulative impact of PNAG NPs and NO co-delivery has not yet been established; therefore, the synergistic effect on full-thickness skin wound healing has been investigated here.

2. Experimental

2.1 Materials and methods

2.1.1 Materials/chemicals. The following materials were used: acryloyl chloride (96%) stabilized with 400 ppm phenothiazines and divinylbenzene (Alfa-Aesar), glycine (98%), hexadecane (HD) anhydrous (Sigma Aldrich), chloroform, ethyl acetate, 1,4-dioxane (99%) extra pure, SDS (90%) (Merck), 2,2-azobisisobutyronitrile (AIBN, 98%), and sodium nitroprusside (SNP) (SRL). Standard cell culture reagents such as DMEM and foetal bovine serum (FBS), penicillin–streptomycin cocktail, and gentamicin from Gibco; and 3-(4,5-dimethylthiazol-2-yl)-2,5-diphenyltetrazolium bromide (MTT; >99.9%) were purchased from Himedia. Ultrapure water (18.2 M) was obtained from Pure Lab Ultra water system (ELGA, High Wycombe, United Kingdom) and used for all sample processing. All other analytical grade reagents, such as glycerol, petrolatum, wax, and mineral oil were obtained from Sisco Research Laboratories (SRL) Pvt. Ltd, Mumbai, India and were used without further purification. The detail of the formation of the nanomedicine has been filed for the Indian patent (patent application no.: 02311051276, date of filing: 31-07-2023).

2.2.1 Synthesis of NAG monomer. *N*-Acryloyl glycine monomer (NAG) was synthesized through a modified approach and converted into PNAG NPs.[20,32] The synthesis procedure is elaborated in the ESI.†

2.3.1 Preparation of sodium nitroprusside-loaded poly-(*N*-acryloyl glycine) nanoparticles. SNP-loaded poly(*N*-acryloyl glycine) nanoparticles (SP NPs) were fabricated in two steps: firstly, poly(*N*-acryloyl glycine) nanoparticles (PNAG NPs) were synthesized from *N*-acryloyl glycine (NAG) monomer, and then sodium nitroprusside (SNP) was loaded into these NPs. The elaborated fabrication method is discussed under the ESI (ESI, Fig. S8†). The details of the formation of the nanomedicine has been filed for the Indian patent (patent application no.: 02311051276, date of filing: 31-07-2023).

2.4.1 Entrapment efficiency (EE, %) and loading capacity (LC, %). The entrapment efficiency (EE, %) of SNP was measured through the UV-Vis spectra (550 nm) of the supernatant recovered after SNP loading using Griess Reagent using the following eqn (1).

$$\mathrm{EE}(\%) = \frac{\text{weight of SNP in NPs}}{\text{weight of SNP added to solution}} \times 100 \quad (1)$$

Loading capacity (LC, %) was measured by dispersing 1 mg lyophilized SP NPs in 5 mL DMSO and incubated for 30 min at 37 °C. After centrifugation at 18 000 rpm, the NO content was measured by a UV-Vis spectrometer, and the percentage of SNP loaded was determined using eqn (2).

$$\text{Drug loading}(\%) = \frac{\text{weight of SNP in NPs}}{\text{weight of SNP loaded NPs}} \times 100 \quad (2)$$

SEM analysis was conducted to confirm the morphology of the PNAG NPs and SP NPs. The EDS and elemental mapping for both the samples were conducted to confirm the loading of SNP in PNAG NPs (see ESI† for detailed methodology).

2.5.1 Characterization of NAG monomer, PNAG, and SP NPs. The NAG monomer, PNAG NPs, and SNP loaded PNAG NPs (SP NPs) were characterized for chemical functionality, crystallinity, particle size, zeta potential (ξ), and elemental mapping and analysis. The ESI† section explains the detailed methods for all characterization methods.

2.6.1 Determination of NO content and NO release profile. The NO content was determined for all the batches of SP NPs. Briefly, 1 mL DMSO and Griess reagent (1 : 1) was used to dissolve 5 mg SP NPs, which were then sonicated for 1 h. After centrifugation at 18 000 rpm, the supernatant was diluted, and the amount of NO was determined by measuring the absorbance at λ = 550 nm (UV-Vis spectrophotometer: Jasco; V-730, JASCO International Co., Ltd, Japan).

NO release was investigated using the dialysis method at a pH of 7.4. The release pattern of NO from the prepared SP NPs was studied for 24 h. Briefly, 5 mg SP NPs in 5 mL PBS (pH 7.4) was dispersed and poured into a dialysis bag and simultaneously immersed in 25 mL dissolution media (PBS pH 7.4, 37 ± 2 °C, 100 rpm), and release was conducted for 24 h. At a predetermined time interval, samples were withdrawn in sink condition, and the amount of NO released was measured by measuring the absorbance at λ = 550 nm, and cumulative drug release (%, CDR) was calculated.

2.7.1 Cytotoxicity study. The cytotoxicity of SP NPs was investigated using an adherent type cell line through the MTT assay.[20] Mouse fibroblast (L929) cells (1×10^4) were grown for 24 h in rich DMEM (DMEM + 10% v/v, FBS), penicillin (100 IU mL^{-1}), and streptomycin (100 μg mL^{-1}) at standard cell culture condition (5% CO_2 at 37 °C). Around 60% of confluence cells were treated with 100 μL SP NPs (0–250 μg mL^{-1}) dispersion and incubated for 24 h. Then, they were rinsed twice with PBS, and 20 μL MTT solution (5 mg mL^{-1} MTT) was added to cells and incubated again for 4 h. The MTT solution was then removed, and DMSO (200 μL) was further added to each well to dissolve formazan crystals and incubated for another 20 min. The absorbance was measured at 570 nm using a plate reader. The data were collected in three distinct biological replicates, each done on a different day, on a different cell passage, and with three repetitions. The cell viability was estimated using eqn (3),

$$\text{Cell viability}(\%) = \frac{\text{OD treatment}}{\text{OD control}} \times 100 \quad (3)$$

where OD is the optical density value recorded using a microplate reader.

2.8.1 Hemocompatibility. Venous blood samples were used to test the hemocompatibility of PNAG NPs. Sodium citrate was used as an anticoagulant in tubes holding whole venous blood.

2.8.1.1 Hemolysis study. Hemolysis was conducted on rat RBCs.[33] RBCs were isolated from whole blood, and a homogenous suspension was prepared by dispersing in PBS (5×10^{10} cells per mL). The hemolytic effects of SP NPs in the concentration range from 1 μg mL^{-1} to 1000 μg mL^{-1} were examined using a spectroscopic test, and the results of the hemolysis caused by 0.1% dispersion of SP NPs were compared with the positive control (0.1% Triton-X 100 in PBS) and the negative control (PBS, pH 7.4). In a 1.5 mL microcentrifuge tube, 500 μL SP NPs nanosuspension from each concentration and 500 μL RBC suspension were placed and incubated for 24 h at 37 °C and stirred at 100 rpm. Then, the samples were centrifuged (4000 rpm for 10 min at 25 °C). By comparing the sample's absorption at λ_{max} = 540 nm with the positive control (Triton X-100) and the negative control (PBS), the percent hemolysis was calculated using eqn (4).

$$\text{Hemolysis}(\%) = \frac{\text{OD treatment} - \text{OD}(-\text{ve})\text{control}}{\text{OD}(+\text{ve})\text{control} - \text{OD}(-\text{ve})\text{control}} \times 100 \quad (4)$$

2.8.2.1 Blood coagulation study. Two blood coagulation pathways were examined to gauge the effect of SP NPs on the blood coagulation cascade. The activated partial thromboplastin time (APTT) and prothrombin time (PT) were evaluated separately after incubating the plasma with SP NPs at 1, 5, 10, 25, 50, 100, and 200 μg mL^{-1} concentrations. The plasma fraction was separated from whole blood by centrifugation (2500 rpm for 10 min, at 25 °C). SP NPs were incubated with isolated plasma for 30 min at 37 °C with constant stirring. The incu-

bated samples were analysed using a coagulometer (Hemostar XF 2.0, Tulip Diagnostics Pvt. Ltd India). Each sample was examined thrice.

2.9.1 *In vitro* wound healing and live dead assay. The scratch wound healing assay is a well-established *in vitro* technique for investigating coordinated cell migration and proliferation in a two-dimensional context. It was employed to assess the regenerative potential of SP NPs within a controlled experimental setting. The detailed protocol adhered to established the methodologies, wherein 2×10^5 L929 cells were seeded per well in a 12-well plate and allowed to culture for 24 h, achieving 80% confluency. Subsequently, a precisely executed linear scratch wound was introduced on the surface of each well using a sterile 20 μL pipette tip. The cells were then subjected to culture conditions with SP NPs, both in the test (supplemented media) and untreated control (without SP NPs) groups, at concentrations ranging from 50 to 200 μg mL^{-1}. Then, imaging at 0 h, 24 h, and 48 h post-scratch was conducted, and the acquired images were analysed using the ImageJ software to calculate the percentage of wound closure area and closure rate, providing insights into the cellular healing dynamics influenced by SP NPs. By adopting the above protocol, further, the live/dead assay on the L929 cell line under *in vitro* condition was conducted using acridine orange (AO) and propidium iodide (PI) method[34] to verify the viability of cells in the presence of SP NPs. Live cells were incubated with acridine orange (1.5 μM) and dead cells with propidium iodide (31.5 μM). Following a 30-minute incubation period, specimens underwent a meticulous PBS washing procedure. Subsequently, cellular scrutiny and imaging were conducted utilizing a state-of-the-art fluorescent microscope (Nikon, A1, Tokyo, Japan), capturing high-resolution visuals.

2.10.1 *In vivo* angiogenesis. *In vivo* angiogenesis tests were performed to examine the vascular sprouting effect of SP NPs using egg yolk angiogenesis assay, as described in the previous report.[35] The fertilized eggs from a certified and trusted vendor (Ramana Hatchery, Varanasi) were purchased in Varanasi, Uttar Pradesh, India. Before the studies, the eggs were first incubated in an egg incubator for 4 days (96 h) in a controlled environment (38.0 ± 0.5 °C and 50–55% humidity). Using the light and shadow approach, the eggs were tested on the day of the experiment to see if successful embryogenesis had occurred. A little examination window was made on the top of the eggshell to determine the embryo development process. Carefully, while preserving the aseptic conditions, suspensions of various dosages of SP NPs (1, 10, and 100 μg) in PBS were added, compared to the reference (treated with PBS), which was examined for 8 h. Images were captured at various time intervals (0, 2, 4, and 8 h) during incubation using a stereo microscope-mounted Magnus camera (Magnus DC10, Magnus Opto Systems India Pvt. Ltd) at a resolution of 10 megapixels. Images were subsequently examined using the Angiotool and FijiJ image analysis tools.

2.11.1 Development of SP nanoformulation and macroscopical evaluation. SP NPs (5% w/w) were used to prepare a nanoformulation that could be applied smoothly to wounds. In an oleaginous ointment base that was made as described in ointment bases (ESI, Table S1†), SP NPs (5% w/w) were disseminated.[36] SP NPs were placed on an ointment slab and triturated with the base ointment using a long, broad-blade spatula. The ointment base had already been made using the melt fusion procedure. Glycerine (5% w/v) was added with the aid of trituration after proper trituration with an ointment base. Then, the formulation was stored in a wide-mouth bottle/ointment tube, placed in a refrigerator (2–8 °C), and filled into a syringe barrel to estimate the drug content further. The formulated SP nanoformulation was evaluated for macroscopic (observational) characterization (ESI, Table S2†).

2.12.1 Physicochemical evaluation of NO-PNAG nanoformulation

2.12.1.1 Nitric oxide content determination. The USP method (USP 40-NF35, 2017) was employed to evaluate the content homogeneity. Briefly, 100 mg SP nanoformulation was taken from the barrel's top (plunger end), centre, and bottom (needle end) parts of the SP nanoformulation filled syringes (ESI, Fig. S1†). They were combined with 5 mL PBS (pH 7.4) and Griess reagent (1 : 3). Then, the mixtures were homogenized at 25 °C for 15 min with 5000 rpm in shield condition. Then, it was filtered using a 0.45 nylon filter. The NO content was calculated using the Griess reagent method after diluting the samples for examination.

2.12.2.1 Nitric oxide release from the nanoformulation. A modified USP apparatus 2 (ESI, Fig. S2†) was employed to evaluate NO release from the SP nanoformulation. Excess SP nanoformulation was placed in a unique sample holder having a 3.14 cm^2 exposed surface area. After flattening, smoothing, and removing the extra material from the nanoformulation surface with a spatula, the precise loaded amount of nanoformulation was calculated by weight. The figure (ESI, Fig. S2†) shows that the sample holding cell was inverted on the static shaft connected to the burette stand. A pre-cut and pre-wetted 0.22 μm pore-size syringe filter membrane (Millipore, Billerica, MA) was placed on top of the nanoformulation and tightened with a rubber band. To reduce shearing stress induced during sample preparation and its potential impact on drug release, the mounted sample holding cell was left stationary inside the dissolution vessel for 30 min. The dissolution test was started by adding 200 mL pre-heated release medium (PBS, pH 6.8, 37 ± 2 °C) to the vessel and stirred with 200 rpm. Using the Griess reagent method, aliquots of the sample (0.5 mL) were obtained at predefined intervals (15 min, 30 min, 1, 2, 4, 8, 10, 12, and 24 h), and the amount of NO released from the SP nanoformulation was calculated.

2.13.1 Biological evaluation of SP nanoformulation

2.13.1.1 Ethical approval. Wistar rats (aged 6 to 8 weeks; obtained from Department of Pharmaceutical Engineering and Technology, IIT (BHU)) were shaved off their flank hair and treated with iodine solution before being put under anaesthesia with ketamine (10 mg kg^{-1}) and xylazine (10 mg kg^{-1}). This work has been performed as per the ethical guidelines. All the animal studies were examined and approved by the Institutional Animal Ethical Committee (IAEC: approval no.

IIT(BHU)/IAEC/2022/078, dated 03/05/2022, registration no. 2123/GO/Re/S/21/CPCSEA), and the use of animals in this work was carried out in compliance with the IEAC's recommendations. Details are mentioned in the ESI† (*in vivo* study, ethics, and approval).

2.13.2.1 Skin irritation and sensitization. The SP nanoformulation was applied to rat skin for a predetermined period to check for any irritation or erythematious reaction. About 4 cm^2 of the intact shaved skin of rats was treated with SP nanoformulation and formulation base of about 1 g, coupled with the positive control (1% formalin solution as a common irritant). The treated area was confined with bandages. 24 h post-treatment, the wrap was removed and washed with water. Then, the skin of the rats was examined visually for any indications of skin irritation and sensitization, and simultaneously, high-resolution camera images were acquired. Rats under experiments were observed for seven more days to check for indications of oedema and erythema. The Draize scoring system (ESI, Table S3†) was used to calculate the skin irritation score using the primary dermal irritation index (PDII), calculated using eqn (5).

$$\mathrm{PDII} = \frac{\mathrm{PDI}}{4} \tag{5}$$

2.13.3.1 In vivo wound healing. The efficiency of SP nanoformulation for wound healing was investigated using Wistar rats. A 10–12 mm, full-thickness cutaneous wound was developed on the back of rats using a 10 mm biopsy punch. The wound was then stitched together using sterile silicone rings. NO is a known inhibitor of platelet aggregation,[37] therefore; we started the treatment post-wounding of day 1 to provide adequate time for hemostasis and fibrin clot formation. The wounds were then topically treated with 100 mg SP nanoformulation. The formulation base and SP nanoformulation were then applied to the wounds of rats on alternate days (1^{st}, 3^{rd}, 5^{th}, 7^{th}, 9^{th}, and 11^{th}). Rats were kept carefully, and wounds were covered with a conventional gauze bandage dressing. The dressing was replaced with a fresh bandage after each application of treatment. A similar process was maintained for the control group.

2.13.4.1 Study of the histology. Deep granulation tissue and cross-sectional full-thickness skin specimens from cicatricial tissue were acquired on the 14^{th}-day post-treatment. Formalin-fixed paraffin-embedded blocks were sectioned in the transverse plane with a section thickness of 5 microns and stained with Mayer's hematoxylin and ethyl eosin and Mallory's Trichrome stain. Mounted sections were analysed with an optical microscope at different magnifications.

2.13.5.1 Immunochemical analysis. Blood serum was isolated from blood, collected at various time intervals (2, 7, and 12^{th} days of post-treatment), each representing the distinct phase of wound healing and kept at −80 °C until further processing. From these serum samples, the levels of IL-6, IL-1β, TNF-α, CRP, and IGF-1 were determined using commercially available enzyme-linked immunosorbent assay ELISA kits. The relative protein concentrations were estimated by recording the absorbance at 450 nm using a microplate reader, and the values of the inflammation markers were estimated and compared with the control sample.

2.13.6.1 Semi-quantitative reverse transcription and polymerase chain reaction (sqRT-PCR). From the excised wound of the control group and treatment groups of day 2, 7, and 14, nearly 1 mm of tissues were collected. RNA isolation was performed by homogenizing the tissue in 1 mL TRIZOL reagent, followed by chloroform extraction. Next, the aqueous layer was collected, and RNA was precipitated using 1 mL isopropyl alcohol and centrifuged at 12 000*g* and 4 °C temperature for 15 min. The RNA pellet was washed 2 times with 70% ice-cold ethanol and suspended in diethyl pyrocarbonate (DEPC)-treated water. After RNA quantification, 1 μg RNA was used for cDNA synthesis using oligo dT sequence and reverse transcriptase polymerase as per the manufacturer's protocol. Afterward, PCR was conducted using KiCqStart® (Sigma) primer for biomarker target gene PECAM-1 (forward primer sequence 5′-AAACCACAATTGAGTACCAG-3′ reverse primer 5′-ACTTAGCTTGACGTTCTTTG-3′), VEGFA (forward primer sequence 5′-GATAGAGTATATCTTCAAGCCG-3′ and reverse primer 5′-CTCATCTCTCCTATGTGCTG-3′), KDR (forward primer sequence 5′-AAACTGGATAAAATGGGCG-3′ and reverse primer 5′-AGCCTTTTAGGTAGAGTCAG-3′) and housekeeping gene GAPDH (forward primer sequence 5′-TCGGAGTCAACGGATTTG-3′ and reverse primer 5′-CAACAATATCCACTTTACCAGAG-3′) as the reference using Taq polymerase (TAKARA R001A) with 35 repetitive cycles of denaturation at 95 °C for 25 s, annealing at 59 °C for 30 s, and extension at 72 °C for 35 s, followed by final extension at 72 °C for 7 min. PCR products were run on 2% agarose gel, and dosimetry calculation was performed.

2.14.1 Statistical analysis. The independent Student's *t*-test and one-way ANOVA with the Tukey test were used to statistically analyse the *in vitro* and *in vivo* data using Origin software (OriginLab Corporations, Northampton, USA). Statistical significance was determined using a *p*-value of 0.05. The data are presented as mean ± SD.

3. Results

3.1 Characterization of SP NPs

NAG monomer was synthesized using a modified procedure (ESI, Scheme S1†) with 64.21% yield, the chemical functionality was confirmed through NMR [^{1}H NMR (ESI, Fig. S3†) and ^{13}C NMR (ESI, Fig. S4†)] spectroscopy and FTIR spectroscopy (ESI, Fig. S5†), and the crystalline nature of NAG monomer was confirmed through XRD (ESI, Fig. S6†). Unlike glycine, which reacts with ninhydrin to give a vibrant violet, it reveals the lack of a free amino group (ESI, Fig. S7†). The NAG monomer and PNAG NPs were tested for free amino groups using ninhydrin reagent that showed the lack of free primary amine groups and is free from glycine contamination.

Further, this monomer is used to synthesize PNAG NPs (ESI, Fig. S8†), formulated with raw SNP, which results in the

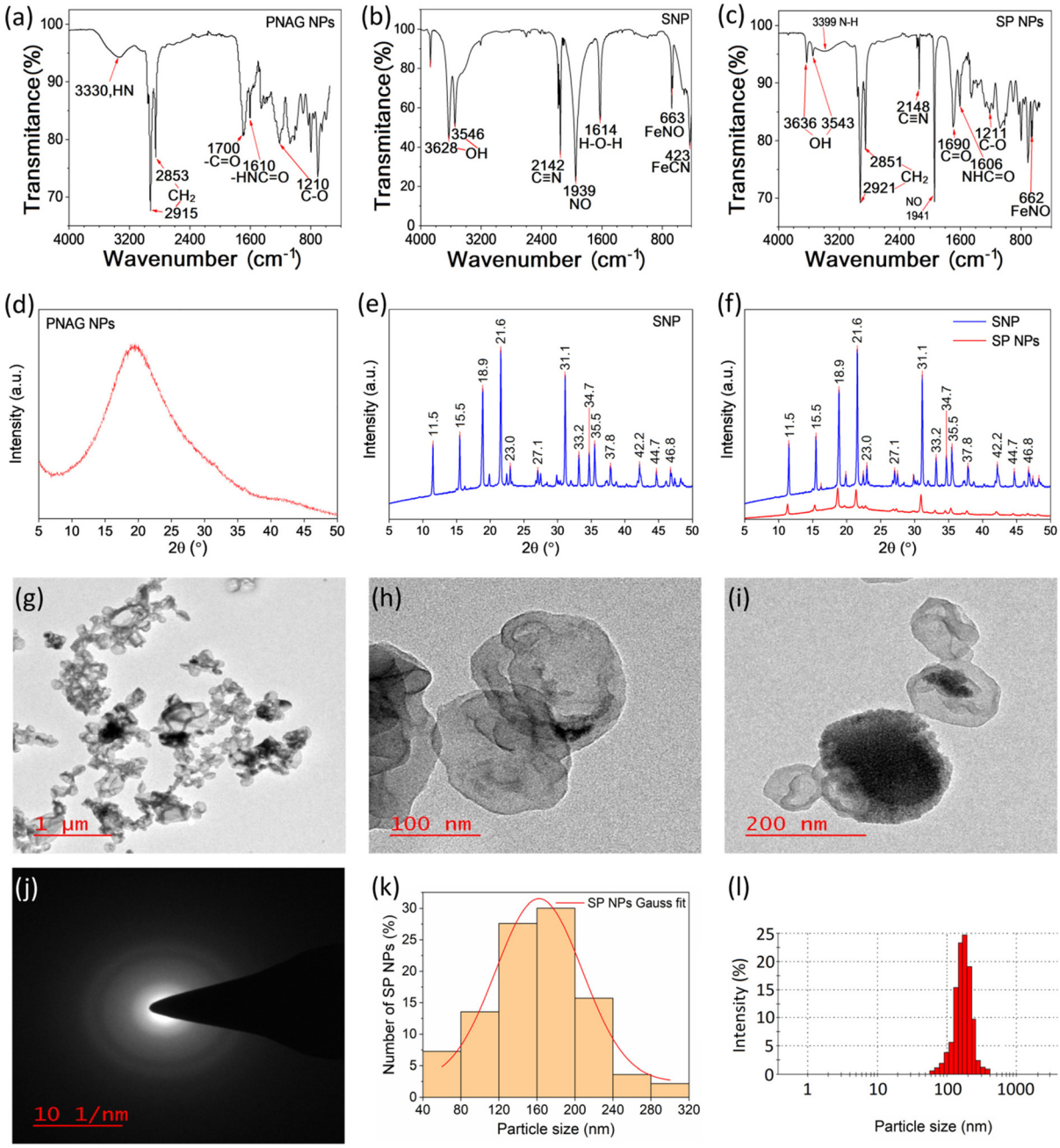

Fig. 1 Characterization of SP NPs. FTIR spectra of (a) PNAG NPs, (b) sodium nitroprusside (SNP) and (c) SP NPs. The XRD pattern of (d) PNAG NPs, (e) SNP and (f) SP NPs. TEM images of SP NPs (g–i), SAED pattern (j) and particle sizes (k) were calculated from the TEM images (number of particles >400) and DLS (l).

formation of SP NPs. The functional groups present in synthesized PNAG NPs (Fig. 1a and ESI, Fig. S9†), raw SNP (Fig. 1b), and fabricated SP NPs (Fig. 1c) were confirmed through FTIR and compared for the loading of SNP in the PNAG NPs FTIR spectrum of SP NPs, which reveals the characteristic distinct bands for the –C≡N and –NO appeared at 2148 cm^{-1} and 1941 cm^{-1} (Fig. 1c), respectively, which are characteristic of SNP (2142 cm^{-1} and 1939 cm^{-1}) loading, confirming the fabrication of SP NPs.[38,39] The bands that appeared at 3628–3546 cm^{-1} of (Fig. 1b) is attributed to the ν_s, OH of SNP, and the bands at 3636–3399 cm^{-1} (Fig. 1c) correspond to the ν_s –OH and $-NH_2$ of SP-NPs, which confirmed the loading of SNP in NPs. The XRD pattern of PNAG NPs, SNP, and SP NPs are shown in Fig. 1. The XRD pattern shows that PNAG NPs are semi-crystalline in nature (Fig. 1d), while raw SNP (Fig. 1e) shows fourteen major peaks at 2θ = 11.5°, 15.5°, 18.9°, 21.6°, 23.0°, 27.1°, 31.1°, 33.2°, 34.7°, 35.5°, 37.8°, 42.2°, 44.7°, and 46.8° in addition to a number of peaks that

correspond to the high degree of crystallinity. On the other hand, the primary diffraction peaks in SP NPs (Fig. 1f: SNP loaded PNAG NPs) appeared at 2θ = 11.5°, 15.5°, 18.9°, 21.6°, 31.1°, 35.5°, 37.8°, and 42.2°, confirming that the SNP are loaded in PNAG particles and the decreased intensity of peaks shows that the crystallinity of SNP reduced after loading into PNAG NPs (Fig. 1f). However, XRD also revealed that PNAG NPs are loaded with SNP. Further, the size and surface morphology of the SP NPs were confirmed through TEM (Fig. 1g–i). The TEM micrograph shows a co-connected (Fig. 1g) and balloon-like structure (Fig. 1h) of SNP-loaded nanoparticles, and the dense core (Fig. 1i) seen in particles supports that SNP is loaded inside the particles. Further, the diffused ring pattern (Fig. 1j) of the SAED confirmed that SP NPs are semi-crystalline in nature, which supports the results obtained from XRD (Fig. 1f). The particle size of SP NPs is found to be in the range of 120–200 nm (Fig. 1k). Particle size results were further confirmed through DLS (Fig. 1l), and the hydrodynamic diameter of particles was found to be *ca.* 167 nm. The stability of the SP NPs was confirmed through the zeta potential (ξ) measurement, and the value was obtained to be −32.8 mV, confirming the excellent colloidal stability of SP NPs. Further, elemental analysis/mapping was performed using EDS through the scanning and focusing of different areas of PNAG NPs and SP NPs, and their corresponding peaks are shown (Fig. 2). Both the elements, Fe and Na are present in SP NPs while the same are absent in PNAG NPs; this again confirms the loading of SNP into PNAG NPs and the successful formation of SP NPs. In the EDS spectrum, the quantitative estimation of Fe, Na, O, N, and C for PNAG NPs and SP NPs is shown. The SEM images and elemental mapping images of PNAG NPs (Fig. 2a1–g1) and SP NPs (Fig. 2a2–g2) are shown. The elements overlay for PNAG NPs found to be 92.9 (Fig. 2b1), 2.04 (Fig. 2c1), 4.84 (Fig. 2d1), 0.0 (Fig. 2e1), 0.21 (Fig. 2g1), and for SP NPs, 79.12 (Fig. 2b2), 1.38 (Fig. 2c2), 1.26 (Fig. 2d2), 7.66 (Fig. 2e2), and 10.59 (Fig. 2f2)%, respectively, of C, N, O, Na, and Fe. Mapping of C element Fig. 2(b1 and b2), N element (c1 and c2), O element (d1 and d2), Na element (e1 and e2), and Fe element (Fig. 2f1 and f2) and all elemental imaging merged (Fig. 2g1 and g2) are shown for f PNAG NPs and SP NPs, respectively. The elemental mapping of PNAG NPs and SP NPs shows the uniform presence of Na and Fe in SP NPs while the same elements are absent in PNAG NPs. The details of the EDX spectra of PNAG NPs and SP NPs measured in atomic and weight% are listed in the table inset in Fig. 2c and d. Further, elemental mapping results confirmed that the SNP molecules are properly loaded in PNAG NPs.

3.2 Drug content loading/entrapment efficiency and NO release efficiency from SP NPs

After accessing the cytotoxicity of PNAG NPs in mouse fibroblast (L929) cells (ESI, Fig. S10†), SNP was loaded in PNAG NPs following the method mentioned in the Experimental section. The EE (%) of SNP was evaluated by measuring the amount of SNP that remained in the supernatants and found that almost 40.97 ± 1.52% SNP was loaded in PNAG NPs, resulting in nearly 4.86% of absolute NO loading. SNP is a hydrophilic molecule and is entrapped in hydrophilic PNAG

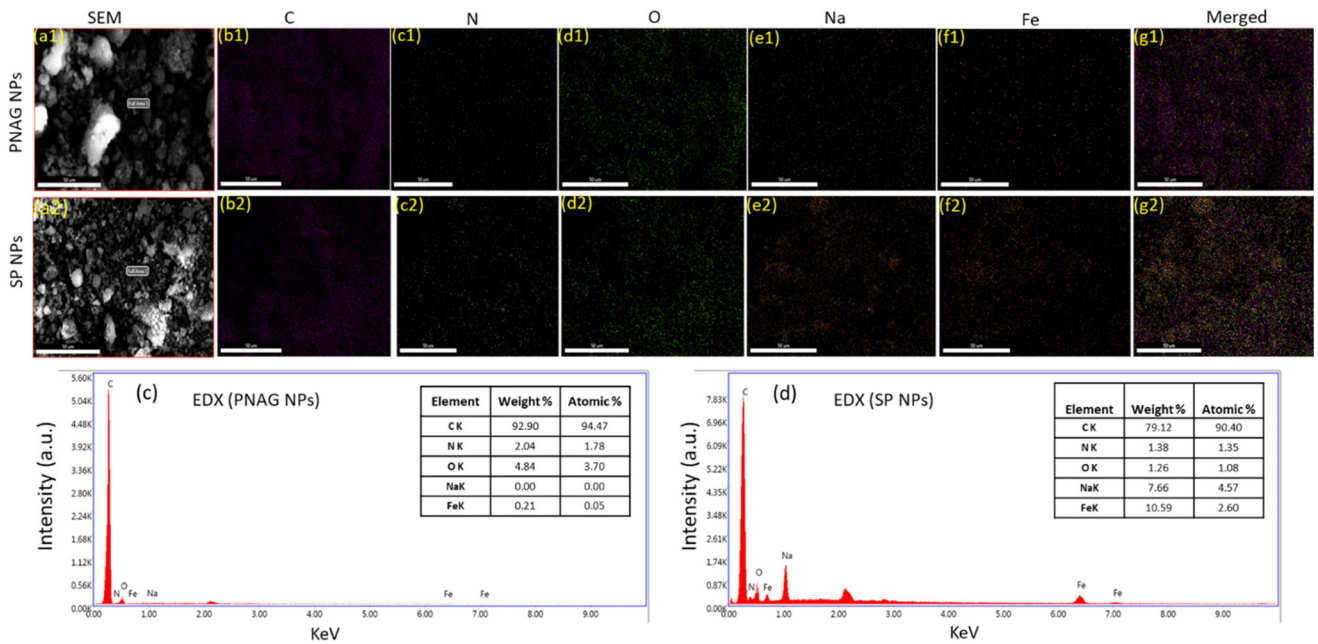

Fig. 2 SEM Images and elemental mapping images of PNAG NPs (a1–g1) and SP NPs (a2–g2). Elements overlay for PNAG NPs, 92.9 (b1), 2.04 (c1), 4.84 (d1), 0.0 (e1), 0.21 (g1), and for SP NPs, 79.12 (b2), 1.38 (c2), 1.26 (d2), 7.66 (e2), and 10.59 (f2)%, respectively, of C, N, O, Na, and Fe. Mapping of C elements (b1 and b2), mapping of N elements (c1 and c2), mapping of O elements (d1 and d2), mapping of Na elements (e1 and e2), and mapping of Fe element (f1 and f2), and all elemental imaging merged (g1 and g2), in the sample of PNAG NPs and SP NPs, respectively. (c) EDX for PNAG NPs and (d) EDX for SP NPs formulation. The inset of (c) and (d) represents the percentage of element presents for the corresponding sample.

NPs easily. Simultaneously, the LC (%) of PNAG NPs for SNP is found to be 48.23 ± 5.63%. The quantification of the NO content was done using UV-Vis spectroscopy using Griess reagent for the unit weight of SP NPs and found to be 98.29 ± 2.79%, which is equivalent to 1.59 ± 0.04 μmol mg^{-1} of SP NPs.

Further, SNP was loaded in PNAG NPs, enabling the release of NO sustainably. The rate of NO release in PBS (pH 7.4) was quantified using the Griess reagent method. The real-time NO release profile and plot of the total NO release in percentage are shown in Fig. 3. It is observed that NO flux was observed to be 19.58 ± 1.97 nmol mg^{-1} min^{-1} within the first 15 min of the start of the release. The total NO content released from the 5 mg of SP NPs within 24 h is 7.95 ± 0.23 μmol, or %CDR is 97.37 ± 8.19%. Further, SP NPs can release NO more in 24 h. It was observed that 47.64% NO is released within one hour from SP NPs. However, the NO release rate continuously decreases with time, as shown in Fig. 3, and follows a sustained release behaviour of 38% of NO over 22 h. Due to the PNAG NPs' hydrophilicity and the SNP's water-soluble characteristics, the release occurred in two stages. In the first stage, NO release was speedy due to the entrapment of SNP on the surface pores of the porous network structure of PNAG NPs. The second stage of NO release is relatively slow because the NO is released from the core part of PNAG NPs.

3.3 Cytocompatibility/cell proliferation and hemocompatibility of SP NPs

For any wound dressing material, it is essential to have cellular proliferative and migratory stimulatory activity along with hemocompatibility. Therefore, low cytotoxicity is one of the essential requirements for using SP NP's proliferative capacity in wound dressings. The cytotoxicity of the present materials was assessed using an MTT assay in mouse fibroblast cell (L929) lines, and PBS was used as the control group. It is noticed that the SP NPs-treated L929 cells survived more than 100% compared to the control, proving that the SP NPs are not cytotoxic. Additionally, with the increase in the concentration of SP NPs, the activity of the cells steadily increased, showing that SP NPs have a potent ability to promote cell growth. The impact of concentrations of SP NPs on the proliferation of L929 cells is shown in Fig. 4a. After the incubation of L929 cells with SP NPs at different concentrations of 2, 10, 20, 50, 100, 200, and 250 μg mL^{-1}, the cell viability (%) relative to the control group is found to be very high as 98.5 ± 11.7%, 101.4 ± 10.0%, 103.4 ± 10.2%, 117.0 ± 10.0%, 163.0 ± 13.0%, 193.3 ± 11.1%, 239.8 ± 10.8%, and 288.7 ± 12.0%, respectively, indicating that the SP NPs exhibits a significant growth-promoting effect on the proliferation of mouse fibroblasts are biocompatible. These studies show that the SP NPs are non-toxic over the concentration range of 2 to 250 μg mL^{-1} and ensure the potential use of SP NPs in *in vivo* wound healing. These results also revealed the cytoprotective effect of NO (Fig. 4a). Further, the hemocompatibility of SP NPs was evaluated by an *in vitro* blood coagulation test (Fig. 4b and c) and *in vitro* hemolysis, which are represented in the consecutive section (Fig. 4d and e).

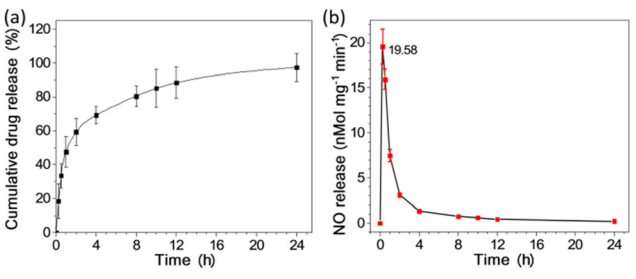

Fig. 3 *In vitro* NO release profile. (a) Cumulative NO release profile (%, CDR). (b) Real-time NO release determination. NO release study was conducted from SP NPs in PBS (pH 7.4) at 37 °C. Data is presented as mean ± SD (n = 3).

3.3.1 Blood coagulation cascade. The anticoagulant properties of the NO-releasing SP NPs to examine the potential biological interactions with the blood coagulation cascade have been studied, and the results are shown in Fig. 4b and c. Using APTT and PT, the *in vitro* anticoagulant activity of the synthesized SP NPs has been studied. The APTT values (Fig. 4b) for SP NPs were found to be 33.0 ± 2.1, 32.7 ± 2.6, 32.5 ± 3.2, 33.0 ± 2.6, 32.6 ± 3.7, 34.7 ± 2.9, and 35.5 ± 1.2 s, for the animals treated at 1, 5, 10, 25, 50, 100, and 200 μg mL^{-1} of SP NPs, respectively. These APTT values marginally deviated from the values reported for the control group of animals (33.0 ± 2.1 s); however, they do not significantly ($P > 0.05$) differ from the control group of animals. Similarly, the SP NPs could not substantially alter the PT values ($P > 0.05$). Therefore, it can be concluded that the coagulation cascade is unaffected by SP NPs in the concentration range of 1–200 μg mL^{-1}, even though the PT time is risen compared to the control. These results suggest that the anticoagulant potential of SP NPs and the enhanced concentrations have no appreciable impact on the PT.

3.3.2 Study of hemolysis. Death can result due to severe blood loss during surgery and trauma. As soon as tissue injury occurs, the wound has to cease bleeding immediately. Consequently, a dressing for wound healing should have high hemostatic[40] or low hemolytic activity. Due to the ease of separation of erythrocytes, the hemolysis assay is routinely considered in studies of novel xenobiotics and membrane-active biomaterials, and the hemolytic activity test provides a versatile approach for swift initial toxicity evaluation. Therefore, the hemolytic activity of SP NPs (Fig. 4d and e) was measured at different concentrations (0 to 1000 μg mL^{-1}) and compared with the results obtained for PBS. Fig. 4d shows the dose-dependent hemolysis caused by SP NPs. The hemolysis extent is found to be 0.06 ± 0.01, 0.08 ± 0.01, 0.29 ± 0.12, 0.39 ± 0.37, 0.49 ± 0.26, 0.53 ± 0.26, and 0.57 ± 0.42% for the SP NPs concentrations of 1, 10, 100, 250, 500, 750, and 1000 μg mL^{-1}, respectively, after 24 h of treatment. It is observed that hemolysis was below 2% at the maximum investigated dose (Fig. 4d), considered safe[41] for topical use or dermal application, and does not cause significant hemolytic activity compared to

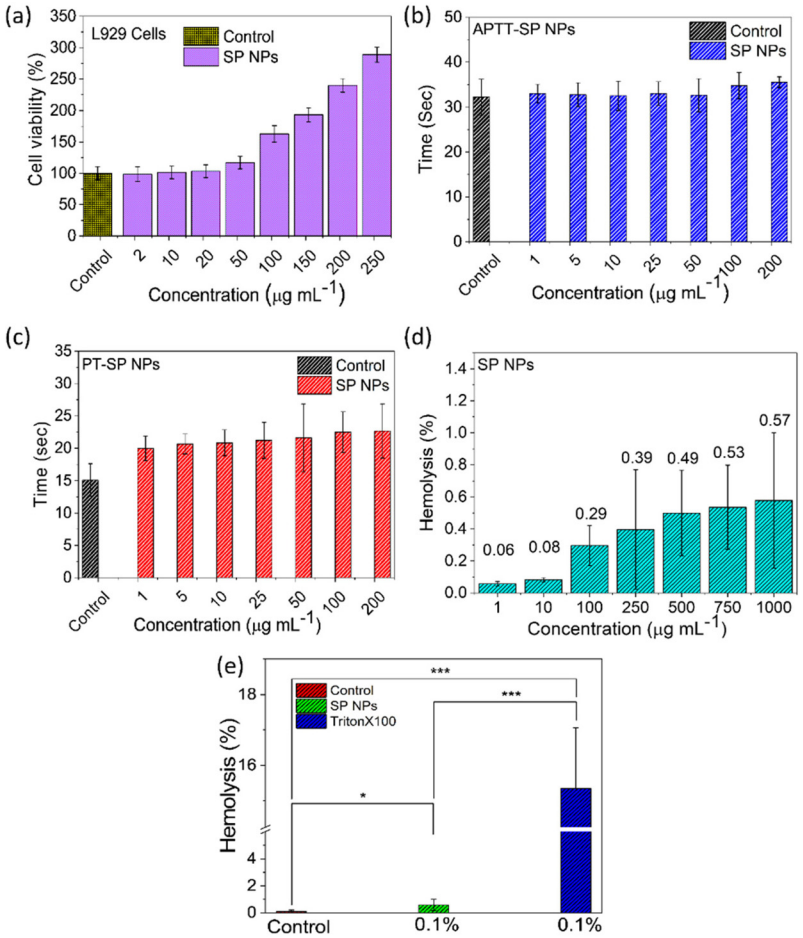

Fig. 4 Cytocompatibility and hemocompatibility of SP NPs. (a) Cytocompatibility assay: treatment of mouse fibroblast (L929) cells with SP NPs shows proliferation instead of cytotoxicity ($P < 0.05$). (b) Activated partial thromboplastin time (APTT) and (c) prothrombin time (PT) tested using different concentrations of SP NPs in the range of 1–200 μg mL^{-1} and compared to the control group (PBS-treated group) ($p > 0.05$). Data are presented as mean ± SD ($n = 3$). Hemolytic effect of SP NPs (4d and e) on rat RBCs. (d) Dose–response curves of hemolysis caused by SP NPs with concentrations ranging from 1 to 1000 μg mL^{-1} ($p > 0.05$). (e) SP NPs show less than 1% hemolytic activity, even at the highest tested concentration (1000 μg mL^{-1}), and hemolysis occurred in rat RBCs by SP NPs dispersion (0.1% w/v in PBS) compared with Triton-X 100 (0.1% v/v, positive control) against rat erythrocytes. Positive control shows ~15% hemolysis, while SP NPs show ~0.57% ($p < 0.05$).

Triton X-100, which causes 15.34 ± 1.71% hemolysis at 0.1% v/v concentration (Fig. 4e). The reason behind high hemolysis caused by adding a detergent like Triton X-100 at 0.1% (v/v) is that it completely hemolyzed the cells and haemoglobin was released, which consequently showed high hemolysis (Fig. 4e). It can be noted that positive control shows ~15% hemolysis, while SP NPs show ~0.57% hemolysis, which is relatively lower than the hemolysis caused by the positive control. Thus, it can be concluded that the SP NPs can be used effectively for wound healing.

3.4 *In vitro* wound healing and live dead assay

The ability of SP NPs to promote wound healing is thoroughly examined by establishing the fibroblasts' migration assay to the wounded area (Fig. 5). The outcomes of a scratch wound healing experiment are shown in Fig. 5(a)–(c), which demonstrates the migration of mouse fibroblast (L929) cells in the presence and absence of SP NPs. In comparison to untreated cells, SP NPs-treated L929 cells migrate more swiftly in the direction of the scratched area (Fig. 5a). Observations from the results conclude that even after 24 h of treatment, none of the group's scratch gap was filled, even though fibroblasts were present in each group in disproportionately huge numbers. However, the treatment group received SP NPs at a concentration of 200 μg mL^{-1}, which covered the scratch gap up to 70.0 ± 26.4%, compared to the control group (21.2 ± 6.2%), indicating that the filling rate is approximately 3.3 times higher. As the doses of SP NPs increased, the other treatment groups also exhibited dose-dependent impact, which showed a reduction in the scratch gap or increased coverage. For SP 50 μg mL^{-1} and SP 100 μg mL^{-1}, the scratch gap coverage for treatment groups was found to be 53.4 ± 28.9 and 60.2 ± 31.4%, respectively. The scratch gap of the control group (PBS) was only significantly narrow after 48 h incubation, and the

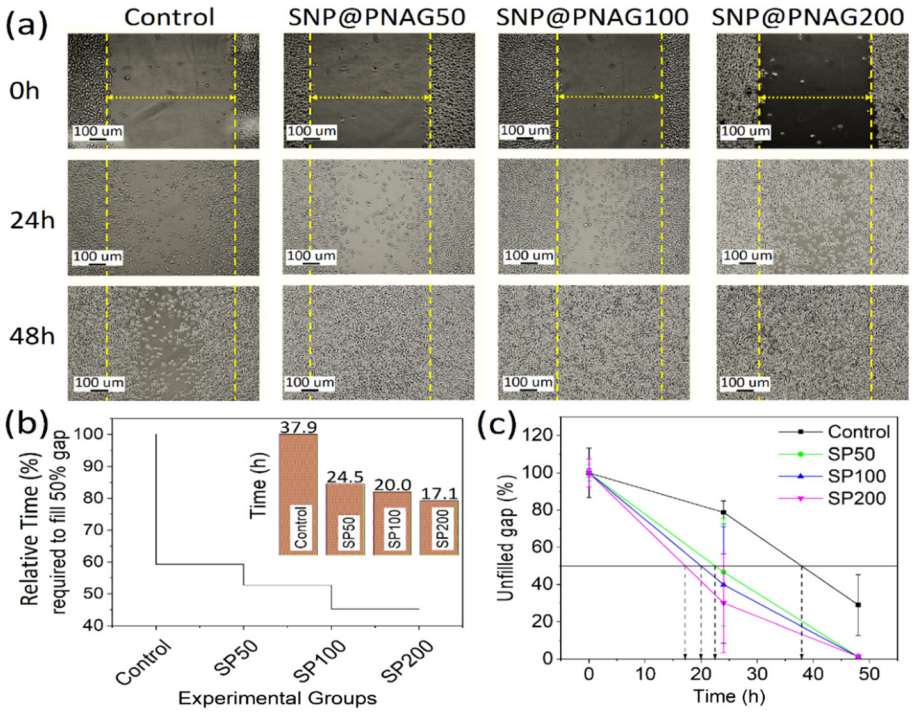

Fig. 5 Scratch wound assay. (a) Microscopic images of scratch wounds created in mouse fibroblast (L929) cells after being treated with SP NPs at concentrations of 50 μg mL^{-1}, 100 μg mL^{-1} and 200 μg mL^{-1} compared to the control at 0, 24 and 48 h. Images were taken at 10× magnification, and the scale bar shows 100 μm. (b) The time taken for cells to fill a 50% scratch gap determines how quickly cells migrated towards the scratch gap. (c) Remaining scratch area to be covered by cells.

gap covered (%) at this stage was found to be 71.0 ± 16.3%. Although the scratch gap of the untreated group showed wounds not wholly closed and some parts remained to fill, the scratch gap of all treatment groups at the concentrations of SP NPs of 50, 100, and 200 μg mL^{-1} were found to be filled (see Fig. 5).

Further, the live/dead assay of the L929 cell line was performed by treating the cells with 50, 100, and 200 μg mL^{-1} SP NPs, and the results were compared with the PNAG NPs (100 μg mL^{-1}). The fluorescent microscopy images after treatment were acquired and the results confirmed (Fig. 6) that the loading of NO in PNAG NPs enhances their viability with negligible sign of toxicity in the form of death of cells, as observed at day-1 (Fig. 6a) at all treatment concentrations. However, on day-3 (Fig. 6b), the PNAG NPs show some extent of apoptotic cell death, while all other concentrations of SP NPs are safe and do not induce the death of L929 cells.

3.5 Angiogenesis (chick embryo membrane assay: CEMA)

Angiogenesis can be precisely characterized as the process whereby new blood vessels emerge and proliferate from pre-existing vascular structures.[42] CEMA is one of the most used models for assessing *in vivo* angiogenic activity.[35] Chick embryos are incubated for 8 h with SP NPs (1–100 μg mL^{-1}) and without SP NPs (reference embryo) show the development of blood vessels. Developed blood vessels are observed at the 8^{th} h compared to the initial stage. The CEMA test in Fig. 7 depicts vascular sprouting or angiogenesis under the influence of NO released from SP NPs compared to the reference embryos. Fig. 7b–g shows the quantitative assessment of vascular development in the treatment embryos under the influence of SP NPs, and in the untreated reference, embryos were estimated using explant area, vessel length, vessel area, total number of junctions, total number of endpoints, and average vessel length. The quantitative data demonstrates that SP NPs treated at 1 and 10 μg mL^{-1} caused a significant rise in the development of blood vessels, while at 100 μg mL^{-1} exhibits adverse effects (seen as the development of distorted and damaged vasculature: Fig. 7a, SP 100) at higher concentrations. These findings assured that the SP NPs could have both pro-angiogenic or anti-angiogenic effects, depending on the dosage used, both *in vitro* and *in vivo*.

Experimental outcomes depict (Fig. 7a) that the chick embryos treated with SP NPs at 1 μg mL^{-1} have exhibited better development than the reference embryos. The embryos treated at 10 μg mL^{-1} showed flushing of blood vessels along with dilation for up to 4 h, while at 8 h, the flushing subsided, and vessels tended to reach their normal stage. On the other hand, embryos treated at a higher concentration (100 μg mL^{-1}) show no flushing, but after 2 h, damaged blood vasculature is observed, and after 4 h, the vasculature tends to revert to normalize anatomy and developmental stage; thus, it can be concluded that this distortion is temporary and may occur due to the access availability of NO (Fig. 7a).

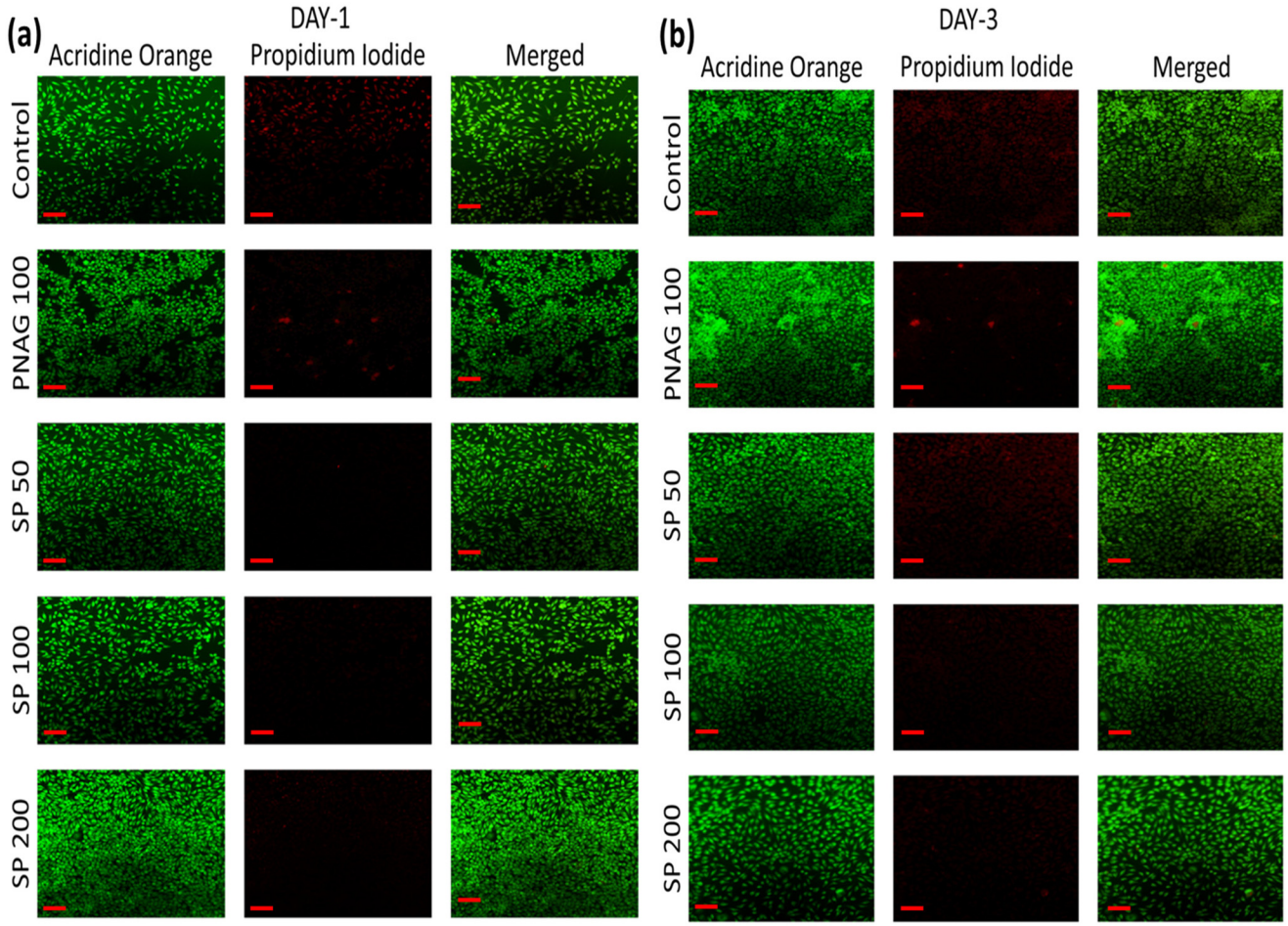

Fig. 6 Live/dead assay study: figures displaying illustrations of live and dead L929 cells, after day 1 (a) and day 3 (b) of treatment with the control, PNAG at 100 μg mL^{-1}, SP NPs at 50, 100, and 200 μg mL^{-1}. Scale bar = 100 μm. Cells were stained with acridine orange and propidium iodide.

The overall region in which blood vessels are developed is called the explant area (Fig. 7b). Embryos treated at lower concentrations of SP NPs (1 and 10 μg mL^{-1}) show a significant increase (158.6 ± 5.5% and 173.6 ± 7.9% of the initial area, respectively) compared to the reference (135.0 ± 8.7% of the initial area of reference). In contrast, the explant area of embryos treated with 100 μg mL^{-1} significantly decreased from 100% (initial explant area) to 95.7 ± 5.7% for the first 2 h. However, after 2 h, it maintained the normal anatomy of the explant area and continued to follow the trends of the reference embryo, and at the end of the 8^{th} h, it was found to be 114.0 ± 6.7% of the initial area.

Vessels area is the total surface area of blood vessels occupied in the explant area. The general trend increases the vessel area as the blood vessels develop and grow. In our experiment, each group's vessel area (Fig. 7c) increased by 113–173% of the initial vessel area. The vessels area measured at 8 h is found to be 121.8 ± 8.7, 166.9 ± 5.7, 173.7 ± 8.3, and 113.3 ± 6.1% of the initial vessels area of reference, and the treatment group treated with SP NPs at a concentration of 1, 10, and 100 μg mL^{-1}, respectively. Herein, the vessel area in embryos treated at high concentrations is lower than in the reference group. Therefore, these findings imply that the SP NPs have both pro-angiogenic and anti-angiogenic effects, depending on the dosage. Further, the junctions are the places from where a new blood capillary starts to arise. In our experiment, we observed an increase in the number of junctions. The highest junction density has been found in embryos treated at 10 μg mL^{-1}, followed by 1 μg mL^{-1}, reference, and 100 μg mL^{-1} (Fig. 7d). Total vessel length is the sum of lengths of blood vessels found in the explants area. The total vessel length (Fig. 7e) was measured. At the 8^{th} h of post-treatment, it has been found a significant increase in embryos treated with 10 μg mL^{-1} of SP NPs (187.9 ± 9.4). However, a non-significant increase (142.2 ± 5.7) is found at 1 μg mL^{-1}, while a significant decrease (123.8 ± 6.6) is found at higher concentrations (10 μg mL^{-1}) compared to the reference embryos (140.0 ± 8.6).

The average vessel length (Fig. 7f) is highest in embryos treated with 10 μg mL^{-1}, followed by a decreasing order at 1 μg mL^{-1}, reference, and 100 μg mL^{-1}. From the above results, it is clear that the embryos treated with 10 μg mL^{-1} show the formation of large blood vessels, while the embryos treated with 100 μg mL^{-1} formed smaller blood vessels.

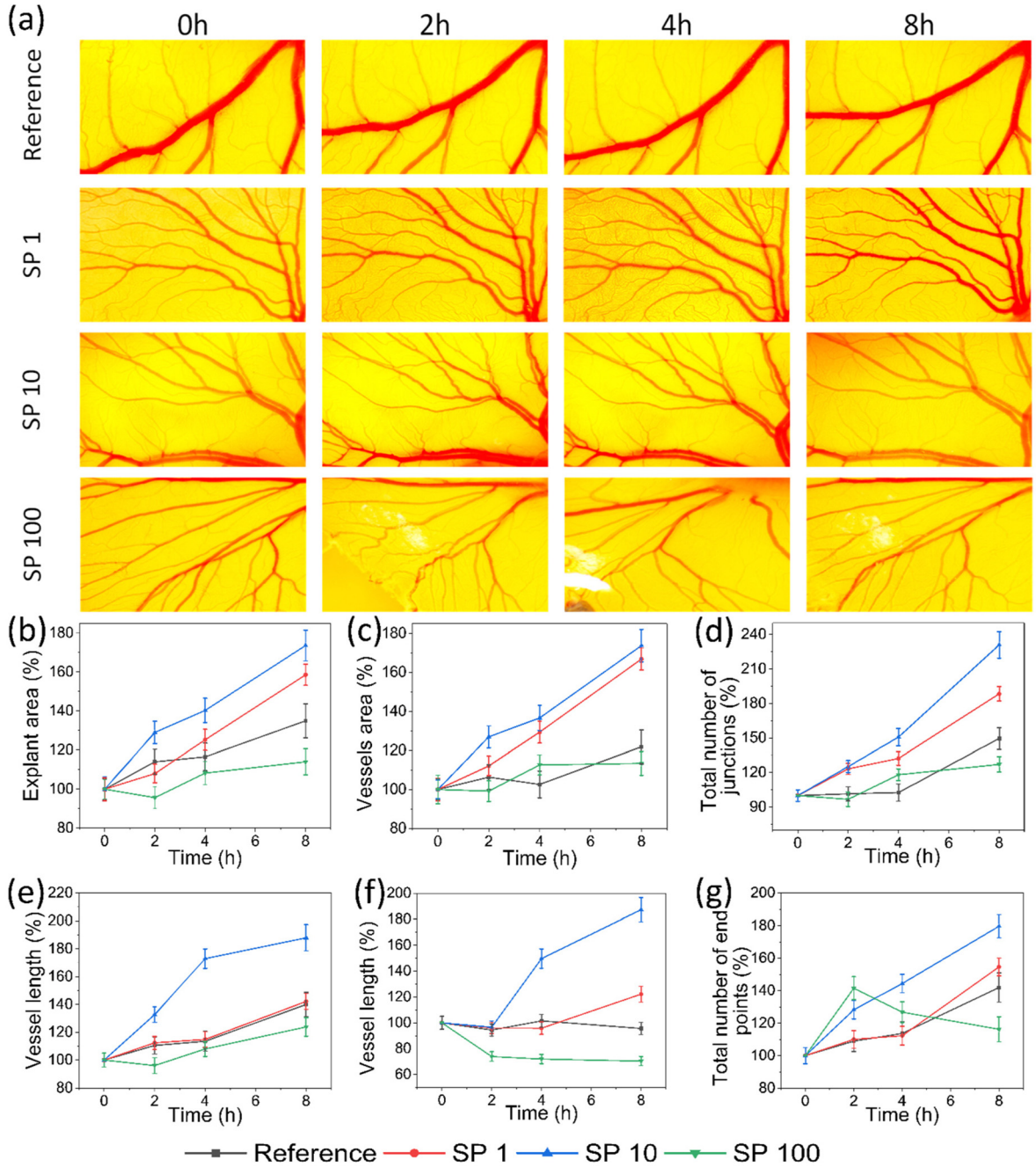

Fig. 7 *In vivo* chick embryo angiogenesis assay (CEMA): (a) determination of the effect of SP NPs on the formation and development of blood vessels in a chick embryo model. Corresponding quantitative assessment of vascular development: (b) explant area, (c) vessel area, (d) total number of junctions, (e) vessel length, (f) average vessel length, and (g) total number of endpoints (all images were taken at 10× magnification using a stereo zoom microscope).

Further, the highest blood vessel endpoints (Fig. 7g) are found in embryos treated with 10 μg mL^{-1}, whereas a decreasing order of blood vessel formation is observed once it was treated with 1 μg mL^{-1} SP NPs, reference, and 100 μg mL^{-1}. It can be noted that the embryos treated with 100 μg mL^{-1} SP NPs show a complex phenomenon within the first 2 h of treatment. At the same time, the highest endpoints were recorded after 2 h of treatment, such as the endpoints decreased and the blood vessels fused.

3.6 SP nanoformulation

To modify the SP NP's consistency and ease of application on the wounds, the SP NPs were mixed with the oleaginous base, one of the most often used ingredients in ointments. The

nanoformulation was examined to check for phase homogeneity, aggregation, and discolouration. It seemed uniform, white to off-white, smooth, and devoid of aggregation (ESI, Table S2†). Results further indicate that the SP nanoformulation had mean content uniformity of 97.29 ± 7.54% for the samples taken from the top, middle, and bottom of each nanoformulation-filled syringe. With a small amount of variance (SD 0.2), the pH of the nanoformulation was at the desired level (pH 7). Assessing the impact of pH variations is crucial because it affects the *in vitro* release of drugs[43] and, ultimately, bioavailability.

3.6.1 NO release from nanoformulation. SNP is a hydrophilic drug molecule entrapped within hydrophilic PNAG NPs. Oleaginous bases are used to prepare SP NPs nanoformulation to increase the control over NO release. *In vitro* drug release has been used to determine changes in the formulation's composition and process factors modulating the formulation's *in vitro* and *in vivo* performance (USFDA, 2016). The NO-release profile of SP nanoformulation (37 ± 2 °C, pH 6.8) was also established, and the outcomes are represented as micromoles per milligram (μmol mg^{-1}) of net SP NPs (Fig. 8). The figure (ESI, Fig. S2†) depicts the experimental setup of SP nanoformulation. In the current investigation, the cumulative NO released per unit area is also measured as a benchmark of the release profile for topical administration rather than cumulative percentage release. SP nanoformulation significantly sustains the rate of NO release than SP NPs. The observed percent cumulative NO release is 79.35 ± 4.43% and 97.37 ± 8.19%, respectively, for SP nanoformulations and SP NPs. Within the 1st h of release, around 2.73 ± 0.062 μmol NO was released, which is 43.75 ± 0.99% of total CDR (%) (34.72 ± 0.79% of the total loaded NO content per 5.0 mg of net SP NPs) from the SP nanoformulation, while the rest of ~56.25% of CDR (%) was released gradually in the subsequent 23 h (Fig. 8a and b). These results suggest that releasing all NO content from the SP nanoformulation required more than 24 h while maintaining the therapeutic level at the application site. The highest cumulative NO release rate (nmol mg^{-1} min^{-1} cm^{-2}) was found to be 5.146 ± 0.050 for the first 15 min, while the lowest release rate (0.064 ± 0.003) was observed in the last 12 h, while the SP nanoformulation releases NO at an average 0.276 ± 0.006 nmol mg^{-1} min^{-1} cm^{-2} for 24 h. This shows a controlled and sustained release of NO from the nanoformulation and is beneficial for wound healing.[44]

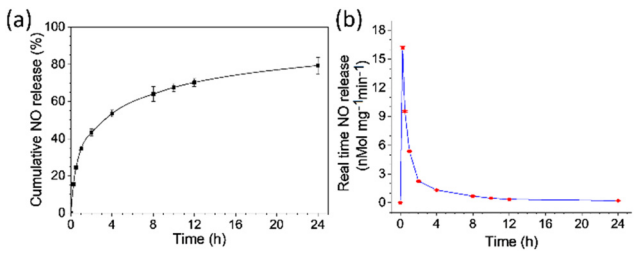

Fig. 8 NO release profile of SP nanoformulation (PBS, pH 6.8, 37 °C, *n* = 3). (a) Cumulative drug release, 79.35 ± 4.43% NO was released from the SP nanoformulation within 24 h, showing controlled and sustained release. (b) Real-time NO release profile.

3.7 Biological evaluation and effectiveness of treatment

3.7.1 Skin irritation. Skin irritation study was performed following the method discussed in the Experimental section. Here, during the study, no animal deaths occurred during the test. In all cases, skin colour is noted for up to 48 h following the dermal treatment (Fig. 9). Finally, aside from the positive group, which exhibits substantial irritation at the site of application of 1% formalin solution, no skin reaction is observed in the control and SP nanoformulation-treated animals at the site for 24 h to 72 h after administration. The PDII score for the positive control group was 2.5, whereas the PDII for the control and SP nanoformulation treatment groups was found to be 0.25.

3.7.2 *In vivo* wound healing. The *in vivo* wound healing studies were performed after describing the materials and the procedure, as discussed in the Experimental section. The findings revealed that the SP NPs exhibited strong cytocompatibility and enhanced cell proliferation, while the SP nanoformulation is non-irritant, both advantageous for the healing of injured skin. Based on the loading capacity of PNAG NPs (48.23 ± 5.63%) and maximum NO content found in SP nanoformulation (97.29 ± 7.54%), the cumulative NO release from SP nanoformulations has been calculated to be 79.35 ± 4.43%. The dose of SP nanoformulation was determined and applied to the wounds. 100 ± 10 mg SP nanoformulation (contains 5% w/w SP NPs) was applied to the cutaneous wounds since this

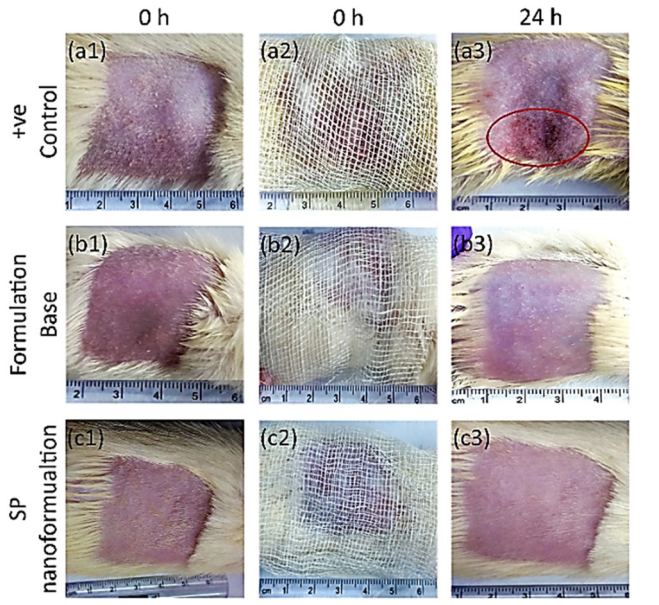

Fig. 9 Photographs of skin irritation study. Positive control (a1) before treatment, (a2) application of 1% formalin solution, (a3) erythema and oedema (shown in red circle) after 24 h of application of 1% standard solution, (b1–b3) control (formulation base) treatment group and (c1–c3) treatment (SP nanoformulation) group not showing any skin sensitivity and irritation after 24 h of treatment of the respective samples.

amount of nanoformulation can be released at a rate of 80.79 ± 0.78 nmol min^{-1} for the first 15 min, 47.67 ± 0.44 nmol min^{-1} for the next 15 min, and 45.57 ± 52 nmol min^{-1} for the next 30 min of nanoformulation treatment. These effective dosages cause nitrosative signalling (for nitrosative signalling, NO concentration must be more than 10 nmol) in the microbes, if any, present at the surface of a wound. After 2 h, these doses can maintain the concentration of NO release sufficiently and below 10 nmol for subsequent 22 h of application, which helps in effective wound healing.[45]

However, the impact of SP nanoformulation on Wistar rats' wound healing was investigated (Fig. 10). It is noted that under normal circumstances, wounds tend to heal with time, and it is a normal phenomenon of body homeostasis. However, we observed that the wound closure in the SP nanoformulation-treated rats moved along swiftly, while wound closure in the control group (formulation base treated group) was noticeably delayed (Fig. 10b). These results suggest that SP nanoformulation can accelerate the wound healing efficiency and can result in full wound closure within 12–13 days of treatment. In contrast to the control group, complete wound closure was not achieved even after 15 days of post-treatment. Consequently, the rate of gross wound closure in the treatment group increased at least 5 days earlier than in the control group. The percentage of wound area was determined to gauge the wound healing process (Fig. 10b). The corresponding percentages of wound closure in the treatment group were found to be 17.6 ± 1.1%, 81.7 ± 0.4%, and 98.3 ± 1.0%, and in the control group, it was found to be 3.6 ± 2.4%, 16.9 ± 4.3%, and 32.9 ± 7.2%, on the 3rd, 7th, and 11th day post-surgery/treatment, respectively. Rat wounds treated with SP nanoformulation heal at a much faster rate than the control for all time points (Fig. 9b). On day 7th, the extent of wound closure is found to be 16.85 ± 4.28% for the control group, whereas it is 81.74 ± 0.41% for the treatment group. These findings showed that the SP nanoformulation has superior healing capacity, which is attributable to NO release. Further, the histopathology studies have been verified and supported the positive

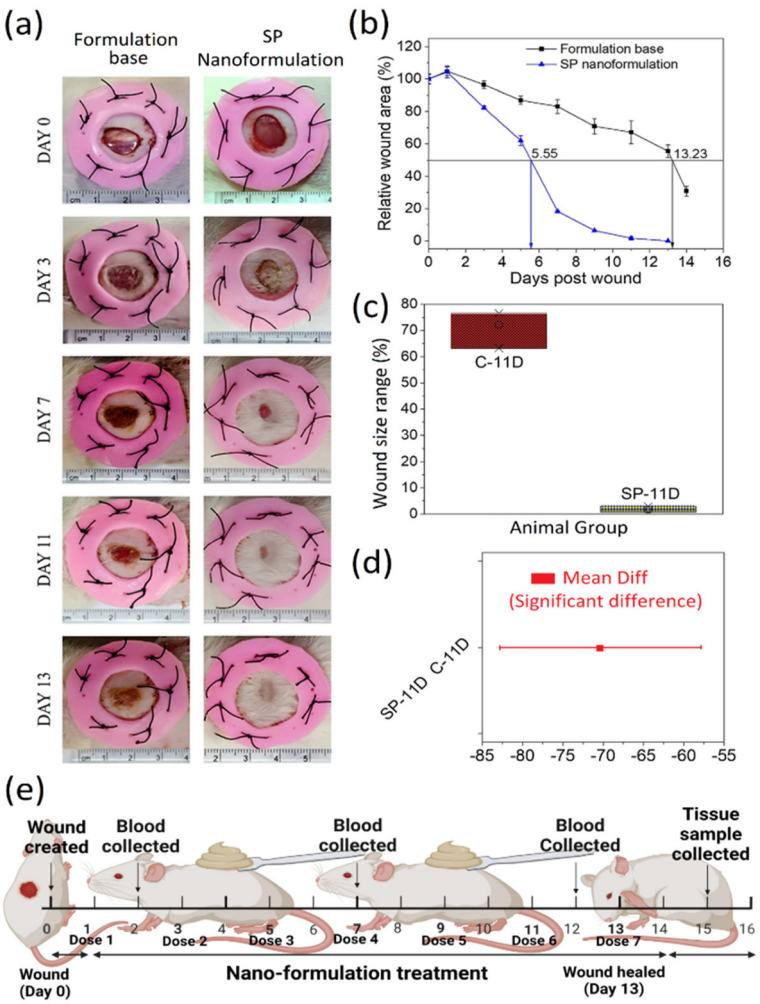

Fig. 10 *In vivo* wound healing assessment: (a) macroscopic images of wounds. (b) Measurement of relative wound area remaining to heal. (c) Range of wound size at 11th day that remained to heal. (d) Significant difference representation of mean wound size on the 11th day using the Tukey test to compare the mean. (e) Time-line of *in vivo* animal experimentation.

effects of SP nanoformulation on wound healing, which is covered in the next section. These findings revealed an apparent propensity for NO therapy to accelerate wound healing.[22,44] However, it can also be observed from the images (Fig. 10a) that after 3rd day post-treatment, both treatment and control groups developed dark red-coloured wound scabs, which prevented the passage of further blood and other fluids.[31] Compared to the control group, inflammatory cells in the treatment group were considerably less. This indicates that on the 3rd day, the early stages of the inflammatory healing process occurred in all the groups, although it progressed more efficiently in the treatment group. This could happen since NO produced by SP nanoformulation can limit the production of inflammatory mediators and stimulate growth factors like IGF-1 (Fig. 12e), which activate NF-κβ and treat the inflammatory phase while accelerating wound healing.[46]

From the images (Fig. 8a), developing layers of skin and wound surrounds are unclear, and these alignments are very loosely maintained because of the inflammatory phase, which promotes platelet clotting and macrophage generation rather than re-epithelialization and dermal remodelling.[31] As anticipated, the granulation tissue production in the treatment group was much higher than in the control groups within the 7th-day post-treatment. On the 13th day, the wound of the SP nanoformulation-treated group is surrounded and covered by fully developed skin layers, while for the control group, a significant wound area remains to be healed.

3.7.3 Histology study. Development of granulation tissue, collagen deposition, and angiogenesis are crucial processes in wound healing and must be carefully managed. An external infusion of NO can regulate these three aspects of wound healing.[44] Skin layer morphology was scrutinized during the healing process and are shown in this section (Fig. 11). The slices of the wounded skin were stained with H&E and Mallory's trichrome stain to show the formation of granulation tissue and re-epithelialization during wound healing. Healthy skin histological features are shown (Fig. 11A: N1, N2, and N3 and 11E: N). After 2nd, 7th, and 14th days post-surgery, the SP nanoformulation demonstrated granulation tissue generation, as shown in Fig. 11A–E.

Further, the morphology of the regenerated tissues can be explained through hematoxylin and eosin staining. From the images of healthy skin (Fig. 11A), a well defined and fully differentiated skin epidermis layer (N1, red arrows), dermis layer with some resting fibroblasts (N2, blue arrow) and active fibroblasts (N2, red arrow), collagen fibres connected with hypodermis, and smooth muscle fibres, skin hair follicle appendages (N2, blue bracket), fat cells and active fibroblasts (N3, red arrow) are identified.

On treatment with the formulation, it is clearly observed that for the 2nd day of wound healing, numerous inflammatory cells (panel C1 and C2 of Fig. 11A, black arrows) are present below the clot edge and the middle region of the wound. From the dermis, the infiltration of neutrophils and other immune cells in the control group indicate that a strong inflammatory reaction occurred (C3 of Fig. 11A, red arrow). Further, in the hypodermis region, it is observed that numerous inflammasomes are present (C3 of Fig. 11A, green arrow), while fewer inflammatory cells (T1 and T2 of Fig. 11A, black arrow) and fibroblast migration (T1 and T2 of Fig. 11A, blue arrow) in the hypodermal wound region occurred in the treatment group. Further, few fibroblasts (blue arrow), along with macrophages (black arrow) migrating to the dermal region and hypodermal region with active (blue arrow) and inactive fibroblasts (orange arrow) along with fewer inflammatory cells (red arrow) in the epidermal region of the wounded site, are observed. It is also noticed that the development of blood vessels started as the tube forming cells are clubbed together (green box) (T3 of Fig. 11A).

For the day 7th of wound healing (Fig. 11B), in the control group, the epidermis is observed to be full of inflammatory cells and messy tissue (C1). Fewer fibroblasts along with large immune cells are present in the dermal region (C2, red arrow). Also, few inactive fibroblasts in the extracellular matrix are present in the hypodermal layer with larger inflammasome (C3) compared to day 2, while a thick epidermis (T1) with numerous blood vessels (T2 and T3, green arrow), immune cells (blue arrow), and dense active fibroblasts (black arrow) are present in the treatment group. On the other hand, epithelial cells with a thicker layer are observed in the treatment group (T3).

On day 14th of wound healing (Fig. 11C), in the control group, the epidermis with diffused basement membrane and thin stratum corneum, stratum granulosum and thicker stratum spinosum (C1), inactive (C2, black arrow) and active fibroblasts (C2, blue arrow), and clumped collagen are observed. These results indicate excessive collagen deposition in the fibrotic tissue with clumped fibroblasts, whereas the treatment group shows the formation of well-defined layers of epidermis including stratum corneum, stratum granulosum, and stratum spinosum similar to normal skin, and the base membrane is also fully developed and differentiated properly (T1). Additionally, elastin-like fibres with active fibroblasts with more euchromatin and basophilic cytoplasm with larger nuclei in the treatment group are formed in the dermis layer (T2). T3 represents the formation of thick collagen bundles with close arrangement and, interestingly, the laying cellular components clearly represent the remodeling and repairing of the tissue.

Further, to investigate the collagen deposition on different days of treatment and the regeneration of tissues, Mallory's trichrome staining was performed. For healthy skin (Fig. 11D and E (N)), thin pink-coloured epidermis and thick blue-coloured collagen bundles having irregular arrangement (N1), irregular thick collagen fibres along with skin appendages (hair follicle) (N2), pinnacles muscle layer between hypodermis and dermis (N3) are observed. For the control group, immature and broken epidermis with diffused basement membrane with minimal collagen deposition are observed (see panels C1, C2, and C3 of Fig. 11D) and Fig. 11E (C-2, C-7, and C-14). Thin collagen bundles (C2 and C-14) with irregular arrangement and numerous immune cells (C-7) are also observed. Further,

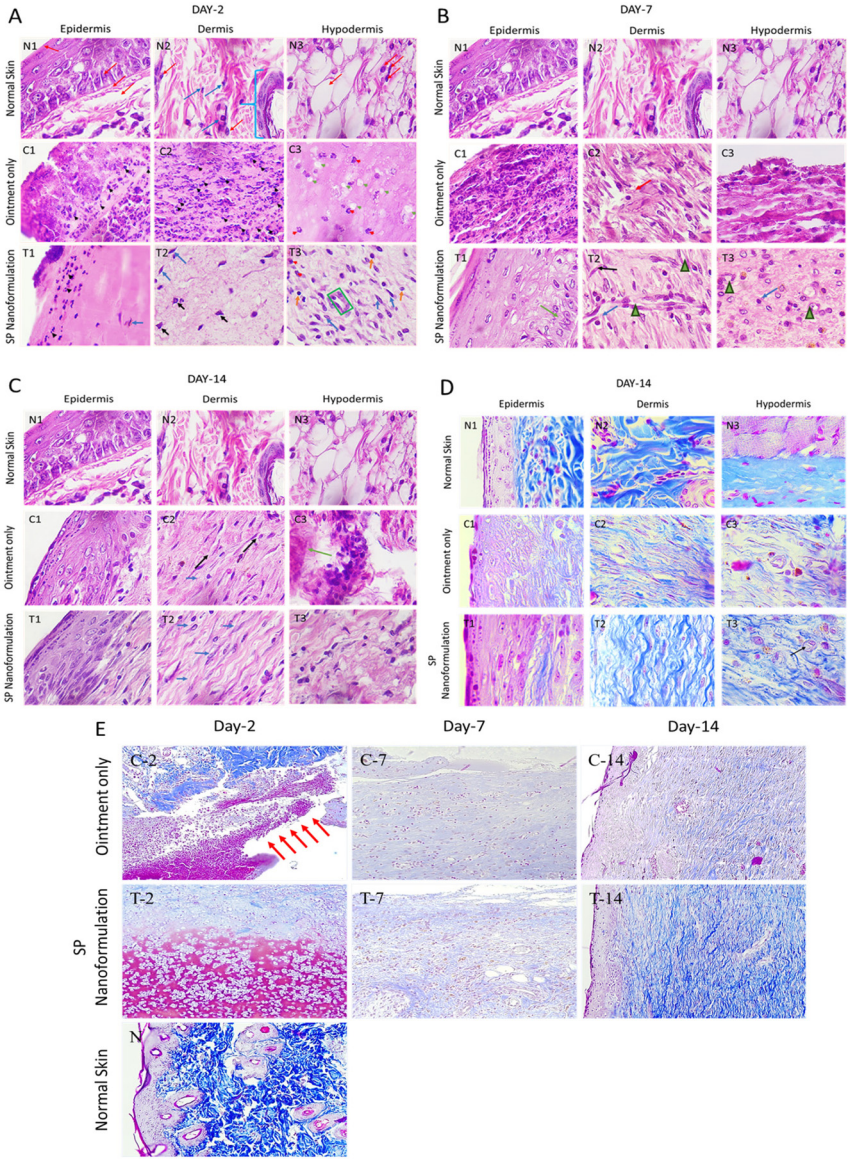

Fig. 11 Histological analysis of skin wound through staining with H & E stain and Mallory's trichrome stain. Histological assessment and comparative histological analysis of the wound on 14th day post-injury with the normal tissue stained with H & E (A, B, and C) on the 2nd, 7th, and 14th day and with Mallory's trichrome stain (D and E) on the 14th day (D) and comparative evaluation on the 2nd, 7th, and 14th day (E). Letters N, C, and T denote the images of healthy skin, control group (ointment base treated group), and treatment group (SP nanoformulation treated group), respectively. Wound healing on day 2 (A), 7, (B) and 14 in the control and treatment group compared to healthy skin. Wound healing comparison on the 14th day using Mallory's trichrome stain (D). (E) Wound healing comparison using Mallory's trichrome stain on day 2nd, 7th and 14th between the control and treatment with healthy skin. Fig. A–D with 100× and E with 20×.

regions with less collagen deposition and with thin irregular collagen fibres are also generated in the control group (C-7 and C-14). On the other hand, for the treatment group (Fig. 11D and E), the well-defined basement membrane with some extent of collagen fibre and well defined layers of epidermis are formed (T1 and T-14). Additionally, thicker collagen bundles with elastin fibre-like arrangement with other cells (T2) are observed. Further, the formation of blood capillaries along with the formation of thicker and more collagen bundles (T-14) with arrangement represents the remodelling of the regenerated tissue (T3). Thus, the SP nanoformulation works well for the treatment of the wounded tissue. The onset of the proliferative phase of wound healing, as well as the proliferation of keratinocytes, endothelial cells, and fibroblasts, can be demonstrated for the use of NO.[31] The exogenous administration of NO in the form of SP nanoformulation thus has better stimulating effects on wound healing. The processes, such as re-epithelialization and collagen deposition, are carried out after the diffusion of NO to the wound tissue region; hence, NO plays a vital role in the wound healing process. Therefore, the present formulation can successfully enhance wound healing. Additionally, angiogenesis promotes

the development of new blood vessels that carry oxygen and nutrients for tissue repair and rebuilding during the healing of wounds.[44]

3.7.4 Wound healing markers and inflammation study. On the inflammatory phase (2nd day), proliferative phase (7th day), and remodelling phase (12th day) of wounding, the levels of cytokines in the blood serum of the treatment and control groups were determined by ELISA to assess the effects of SP nanoformulation. During these phases, the level of cytokines changed significantly, demonstrating the impact of the SP nanoformulation. It is also observed that on the 2nd, 7th, and 12th day of post-treatment, the relative levels of TNF-α, IL-1β, and IL-6 were considerably lower for the treatment group than the control group (Fig. 12). The C-reactive protein (CRP) is a blood protein that is seen in the acute phase and activates the complement. In reaction to inflammatory cytokines, the liver releases CRP into the bloodstream. Herein, after tissue injury, the CRP level quickly rises in response to inflammation and infection, then drops as the wound heals, and the relative CRP levels are significantly lowered in the treatment group com-

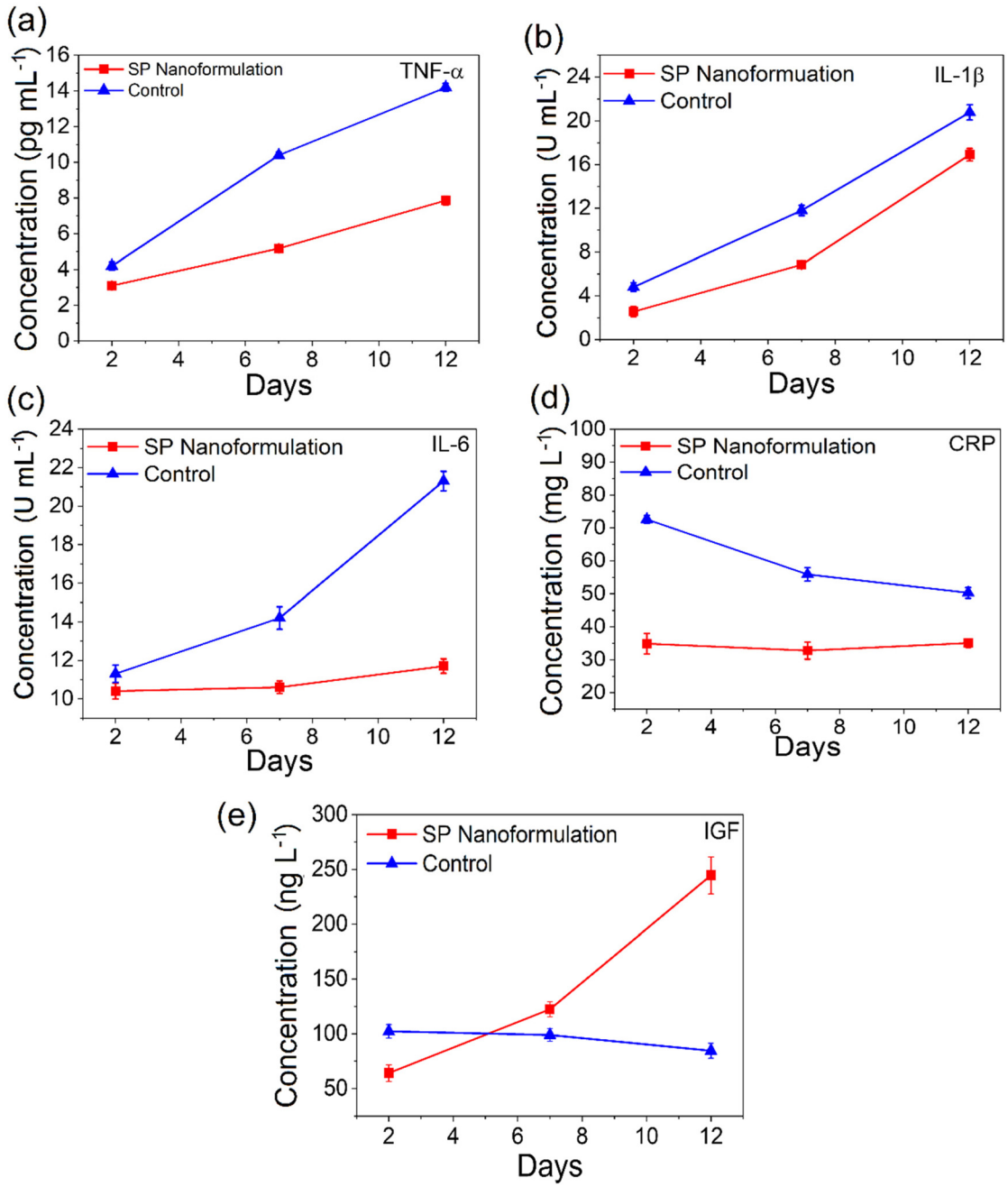

Fig. 12 Wound healing markers analysis by ELISA on the 2nd, 7th and 12th day of post-wounding. (a) TNF-α, (b) IL-1β, (c) IL-6, (d) CRP and (e) IGF-1 levels. Each data point represents the average ± SD of 3 independent determinations ($p < 0.05$).

pared to the control group. On the 7th and 12th day, the IGF-1 levels in the treatment group are considerably higher (Fig. 12e), suggesting a higher likelihood of keratinocyte migration to the injured areas during the proliferation and remodelling phase.[47] In contrast, the control groups have lower levels of IGF-1 while having high levels of pro-inflammatory cytokines (TNF-α, IL-1β, and IL-6). These deterrent effects on the levels of pro-inflammatory cytokines are found due to the regulated NO release from the SP nanoformulation. Thus, it can be concluded that NO functioned as an anti-inflammatory agent, and the SP nanoformulation successfully protects the cells from inflammation *via* controlled-release profiles.[48]

3.7.5 Semi-quantitative reverse transcription and polymerase chain reaction (sqRT-PCR). To study the gene expression during wound healing, an sqRT-PCR study was performed, as mentioned in the Experimental section, and the results have been shown in Fig. 13a–c. Fig. 13a shows the band of gene expression for day 2 (C-2), day 7 (C-7), and day 14 (C-14) for the control group and for day 2 (T-2), day 7 (T-7), and day 14 (T-14) for the treatment group. It can be noted that GAPDH is a housekeeping gene and is used as a reference control in gene expression analysis. Furthermore, in our study, the gene expression analysis by sqRT-PCR revealed that the expression level for the KDR gene is found to be higher in the control group with respect to the treatment group for all the treatment days (see Fig. 13b and c); however, the gene expression difference is non-significant. In wound healing, VEGFA plays a direct and indirect role in the migration of inflammatory cells and keratinocytes by inducing proliferation and collagen deposition in the remodelling phase.[49] VEGFA also interacts with the receptor KDR and mediates the internalization of KDR to the nucleus; finally, the activation of PI3-kinase/AKT occured.[50] The expression of VEGFA is higher on day 2nd and downregulated at day 7th and 14th in the control group at day 2 (see Fig. 13b and c). This high expression could have occurred due to the increased migration of inflammatory cells to the wounded region in the control group. On the other hand, in the treatment group, the VEGFA expression was downregulated on day 2nd of treatment. The expression of VEGFA was observed at the base line on day 7th and increased on day 14th of treatment. These results suggested that the SP NPs formulation have a major role in enhancing scarless wound healing. Similarly, PECAM-1 (CD31) plays a central regulatory role in wound healing as a representative of angiogenesis. However, the increased expression of PECAM-1 is occurred with day of treatment in the control group. In the treatment group, on day 2, the PECAM-1 expression was downregulated, whereas for day 7 and 14 of post treatment, the same increased compared to the control group (Fig. 13). Thus, SP nanoformulation has a regulatory effect on KDR, VEGFA, and PECAM-1 expression for the regeneration of the wounded tissue.

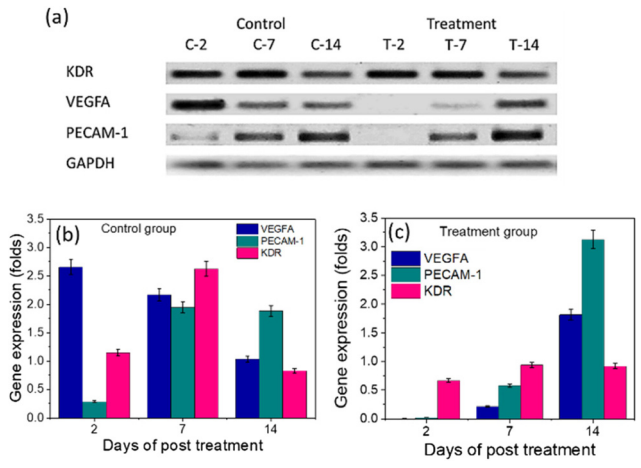

Fig. 13 (a) Relative expression of various genes during wound healing. (b) and (c) represent the gene expression level relative to GAPDH (in folds) for the control and treatment group, respectively, for VEGFA, PECAM-1, and KDR. In the figure, the band of gene expression for day 2 (C-2), day 7 (C-7) and day 14 (C-14) for the control group and for day 2 (T-2), day 7 (T-7) and day 14 (T-14) for the treatment group.

4. Discussion

This study has formulated water-dispersible NO-releasing biosafe advanced polymeric nanoparticles (SP NPs) by free radical polymerization and subsequently loading with SNP. FTIR shows characteristic bands of cyano, NO, and Fe-NO groups at 2148 cm^{-1}, 1941 cm^{-1}, and 662 cm^{-1}, which confirmed the formation of NO-releasing NPs (SP NPs) (Fig. 1c). Many parameters, such as formulation components, manufacturing processes, or process factors including time, temperature, pressure, instrument type, lyophilization, packaging, and storage conditions, have an impact on the average particle diameter of NPs. The particle size requirement and distribution of well-designed nanosystems should be in the submicron range[51] because the interactions between biochemical and cellular components of cells and nanocarriers take place only when particles are typically smaller than 200 nm; these interactions are distinct from those arising from relatively larger particles or implants made of biomaterials.[52] Therefore, using TEM and DLS, the morphology, size, and distribution were examined, and due to an average size of 162 nm (dia), these SP NPs potentially exhibited bioactivity. Herein, zeta potential (ξ),[51] found to be ~−32.8 mV, represents the colloidal stability of the SP NPs. Due to the abundance of anionic carboxylate groups, SP NPs are stabilized by electrostatic repulsion and steric stabilization. Drug loading is crucial when fabricating an NP-based delivery system since low loading requires significantly more formulation for an optimum therapeutic effect.[53,54] Therefore, low drug loading is an obstacle for using nanotherapeutics, necessitating high LC and EE. Herein, high LC (48.23 ± 5.63%) and high EE (40.97 ± 1.52%) were found for SP NPs. The loading of SNP was also confirmed by the elemental analysis of SP NPs, which shows the availability of Fe and Na as metallic components of SNP (Fig. 2). This proves that in fewer doses, SP NPs can deliver more NO. The reason for this high LC and EE are the cross-linking of PNAG NPs

with DVB, which also helps to retain their good water dispersibility. Thus, these SP NPs also have good NO content measured as 98.29 ± 2.79%, equivalent to 1.59 ± 0.04 μmol mg^{-1} of SP NPs.

In vitro release plays several crucial functions during a drug product life cycle from the viewpoint of product quality. Thus, the quality control strategy at the early and late stages of product development guarantees batch-to-batch consistency and uniformity.[55] According to the literature, SNP's mean plasma elimination half-life in aqueous solution is about 2 minutes.[56] In the study of NO delivering and releasing biomaterials, the release time is one of the essential performance parameters. Numerous studies were done to modulate the release of NO.[57–60] The *in vitro* release of NO entrapped on the SP NPs was investigated in PBS at pH 7.4 and temperature 37 ± 2 °C to simulate the intestinal environment and the CDR (%) was found to be 97.37 ± 8.19% within 24 h. Fig. 3 demonstrates that SP NPs successfully regulate and lower the release rate of NO. The requirement for frequent dosages may decrease with persistent NO administration. A regulated NO release is crucial for the actual clinical application of NO-releasing biomaterials.[61] For rapid and long-term pharmacological actions from NO-releasing biomaterials, sustained NO release for at least 24 h is necessary since once-daily dosing for chronic disorders can be manageable.

A successful demonstration of NPs biocompatibility through a series of *in vitro* and *in vivo* tests may evaluate the cytotoxic or immunological impact triggered after their administration is required for the regulatory approval of innovative nanocarriers. An ideal material for a wound dressing should be biocompatible, reduce inflammatory receptivity, manage inflammation, and accelerate wound healing.[46] The clinical availability of nanocarriers for delivering medicines to target diseased tissues more successfully depends on an accurate biocompatibility assessment. It is well known that interactions between cells and biomaterials can lead to protein adsorption and cell contacts, activating host defence mechanisms such as thrombogenicity and inflammation. These reactions may result from the body directly detecting nano-biomaterials or an unintentional release of pro-inflammatory cytokines, which results in cytotoxicity and, subsequently, loss of cell integrity in response to nano-biomaterials.[62] In this work, we found that SP NPs are well tolerated by mouse fibroblasts (L929) cells, exhibiting proliferation (Fig. 4a) and do not cause cytotoxicity while exhibiting acceptable hemolysis (Fig. 4d and e) at the highest concentration (1 mg mL^{-1}) tested for therapeutic purpose and having no adverse effects on the coagulation cascade (Fig. 4b and c). Therefore, the absence of cytotoxicity assures that the potential of SP NPs can be used for *in vivo* application. The experiments showed that SP NPs are biocompatible and have the potential to stimulate cell growth when loaded with SNP, and these findings also pointed to NO's cytoprotective properties. Therefore, our studies demonstrate both the biocompatibility of SP NPs and its ability to promote cell proliferation when loaded with SNP.

Conventional bioequivalence techniques based on plasma pharmacokinetic data sometimes may not be feasible and may not produce relevant results; in such a case, demonstrating the therapeutic equivalence of topical semi-solid therapeutic might be difficult. Suppose two formulations (test and reference) release medication at different rates when compared under the same circumstances and when the case reference data are unavailable. In that case, an *in vitro* release test can reveal the most significant information changes in the microstructure of the two formulations.[43] As a result, the *in vitro* release test is crucial in determining how well a medication product performs.

The role of NO in wound healing is extensively explored.[14] It has been challenging to identify which of NO's functions could modulate wound healing, although the different effects of NO depend on the location and concentration because several elements and modulators affect wound healing. To mimic the cutaneous wound healing processes more closely, sterile silicone rings are stitched around the wound in our investigation, which avoids tissue contraction. This mechanism was utilized to focus on the re-epithelialization process as a crucial stage in wound healing since skin contraction is more evident in murine models of wound healing than in human wounds. We observed that NO treatment promotes tissue repair after damage by direct re-epithelialization (Fig. 10).

Our findings also demonstrated that the topically applying SP nanoformulation to skin wounds in rats supplemented with NO levels slightly above physiological levels and markedly speed up the wound healing process.[47] Notably, by entering the cell and assaulting microbes DNA and cellular machinery, NO is anti-microbial, successfully boosting the host immune system and helping eliminate the microbial burden.[22,58,63,64]

SP nanoformulation enhances wound healing by fostering fibroblast migration and collagen depositions at the site of the injured area. By enhancing fibroblasts' proliferative capability and motility, increased granulation tissue development hastens wound healing.[65] SP NPs significantly increased the number of fibroblasts in the scratched region of a plate, indicating that particles upregulate fibroblasts' mobility and proliferation (Fig. 5), simultaneously not inducing any adverse effect, which may cause toxicity to cells and may result in the death of fibroblasts (Fig. 6). Fibroblasts are crucial in the regeneration of new tissue in wounded regions as they create the groundwork for the keratinocyte's migration and finally the wound healing. When considered as a whole, these findings demonstrated that NO seems to be involved in controlling fibroblast migration and proliferation through interlinked processes, eventually improving wound healing.

Earlier findings concerning the function of NO are encouraging to angiogenesis.[35,66] In comparison to the untreated CEMA, the SP NPs-treated CEMA showed much more significant vascular sprouting (Fig. 7). The quantitative data demonstrates that SP NPs treated with 1 and 10 μg cause a significant rise in the development and maturation of blood vessels, but at a higher dose (100 μg), it exhibits adverse actions during the starting hours of dosing (development of distorted and damaged vasculature). These findings imply that SP NPs have

both pro-angiogenic and anti-angiogenic effects, depending on the dosage. The mechanism of the angiogenic effect can be given in the context that enhancing and recruiting angiogenesis-supporting elements like TGF-β and vascular endothelial growth factor (VEGF) provide enough blood flow toward a healing wound, and NO can support improved wound healing.[65] For instance, TGF-β helps to increase the tissue debridement at the wound site brought on by macrophages and results in encouraging the recruitment of more and more inflammatory cells. Herein, we postulated that by controlling and regulating the interactions among the fibroblasts, inflammatory cells, cytokines, and remodelling proteins, the topical administration of NO-releasing nanoformulation could reduce the time and accelerate the rate of wound healing.[65]

Additionally, the favourable effects of NO on fibroblast migration and proliferation enhanced the effectiveness and accelerated wound healing. The SP nanoformulation with huge potency undoubtedly caused by nanoparticles changes the biodistribution and release of NO (Fig. 8).[67] With the topical administration of the SP NPs nanoformulation, we did not see any adverse effects in the form of skin irritation and sensitivity (Fig. 9), which is in line with another study[65] that showed that topically administered NO-releasing nanoparticles might cause local immunological modulation (Fig. 12) with minor inflammation (Fig. 12). When nitric oxide is released, it can trigger a cascade of events that polarizes macrophages toward a particular type of immune response.[20] The application of polymer nanoparticles in the delivery of NO can make it possible to administer a precise dosage, which would adequately heal the wound in a regulated manner without producing undesirable outcomes such as tissue damage or severe scarring confirmed through the expression of various gene during the wound healing treatment. An important protein expressed during wound healing is VEGFA, which have both direct and indirect effect on wound healing.[49] The relatively higher expression of VEGFA in the control group on day 2 is responsible for the attraction of inflammatory cells, while the level of the same is decreasing in the control group with time, which shows improper healing as VEGFA is responsible for angiogenesis, inflammation, cell proliferation and migration, granulation tissue formation, collagen synthesis and, finally, wound contraction,[49] which is accordingly expressed higher in the treatment group and accelerates the healing process through the abovementioned mechanisms (Fig. 13). The dynamic regulation of KDR gene expression is crucial for orchestrating the angiogenic response during wound healing. The proper control of KDR activation ensures the formation of a functional vascular network that supports the delivery of oxygen, nutrients, and immune cells to the healing tissue, ultimately promoting effective wound repair.[68] Another important aspect of accelerated wound healing is the expression of PECAM-1 molecules, which is involved in the regulation of endothelial cell function and leukocyte recruitment; during the initial stages of wound healing, it is involved in leukocyte recruitment and migration to the site of injury and regulates a critical step in the inflammatory response.[69] The availability of PECAM-1 during the later stage of wound healing is necessary because it also promotes the tissue that undergoes remodeling, and maturation contributes to the maintenance of vascular integrity during tissue repair.[70] Thus, our early outcomes are promising and encouraging to apply these polymeric nanoformulations as regenerative nanomedicines. Additionally, it would be appropriate to carefully examine the suitability of SP NPs and their nanoformulation for long-term, non-healing wounds and for enhancing difficult wound healing. However, long-term investigations are necessary to evaluate the potential consequences of administering SP NPs and its topical nanoformulation on the skin and other tissues.[65,67]

5. Conclusions

The synthesized novel PNAG NPs are loaded with NO donor (SNP) and transformed into NO-releasing PNAG NPs (SP NPs) with high loading efficiency. SP NPs can be used to deliver NO *in vitro* and *in vivo*. The prepared system can release NO in PBS (pH 7.4 and 6.8) for more than 24 h when tested *in vitro*. Cytotoxicity analysis indicated that SP NPs exhibited good biocompatibility in mouse fibroblast (L929) cell line and displayed negligible hemolytic behaviour on rat RBCs. To evaluate the effect of SP NPs on wound healing promotion, we prepared SP NPs-impregnated nanoformulation using an oleaginous ointment base for enhancing the residence time and smooth application. The nanoformulation is non-irritating for rat's skin. Both NO and PNAG NPs show synergistic effects on cutaneous wound healing by enhancing granulation tissue formation, collagen depositions, angiogenesis, and regulating cytokines, chemokines, and other genes responsible in wound healing and may prove superior compared to the available treatment methods. Therefore, SP NPs and SP nanoformulation is a versatile NO-releasing formulation with a promising future in regenerative medicine and is paramount for therapeutic technology.

Author contributions

Prem Shankar Gupta and Kirti Wasnik (conceptualization, investigations, formal analysis, cell based analysis, gene expression, data curation, visualization, software, writing – original draft and writing – review and editing), Sukanya Patra (methodology), Divya Pareek (methodology), Gurmeet Singh (angiogenesis, *in vivo*, histology study), Desh Deepak Yadav (review and editing), Somedutta Maiti (methodology) and Pradip Paik (project administration, supervision, resources, fund acquisition, writing – review and editing).

Conflicts of interest

The authors have no conflicts of interest to declare.

Acknowledgements

The authors acknowledge the fellowships supported by IIT (BHU) MHRD. Instrument facilities of IIT (BHU) and ISLS-CIF have been used for acquiring data like TEM, SEM and FTIR etc. Authors acknowledge the financial supports awarded to Prof. Pradip Paik by DST-Nanomission, India, (ref: SR/NM/NS-1005/2015), Science and Engineering Research Board (SERB), India, (ref: EEQ/2016/000040), I-DAPT Foundation (ref. I-DAPT/IT (BHU)/2023-24/Project Sanction/47), STARS-IISc. Bangalore (ref. MoE-STARS/STARS-2/2023-0318) and IIT (BHU) Seed Grant (Plan-OH 35). Authors also acknowledge the guidance and support provided by Dr Sudip Mukherjee, Assiatnt Professor, School of Biomedical Engineering, Indian Institute of Technology (BHU), Varanasi, India.

References

1 S. Wang, W.-Y. Wu, J. C. C. Yeo, X. Y. D. Soo, W. Thitsartarn, S. Liu, B. H. Tan, A. Suwardi, Z. Li, Q. Zhu and X. J. Loh, *BMEMat*, 2023, **1**, e12021.
2 C. K. Sen, *Adv. Wound Care*, 2021, **10**, 281–292.
3 V. K. Shukla, M. A. Ansari and S. K. Gupta, *Int. J. Lower Extremity Wounds*, 2005, **4**, 7–8.
4 P. Abaffy, S. Tomankova, R. Naraine, M. Kubista and R. Sindelka, *BMC Genomics*, 2019, **20**, 815.
5 J.-D. Luo and A. F. Chen, *Acta Pharmacol. Sin.*, 2005, **26**, 259–264.
6 A. Friebe, P. Sandner and A. Schmidtko, *Naunyn-Schmiedeberg's Arch. Pharmacol.*, 2020, **393**, 287–302.
7 X. Wang, M. Zhang, T. Zhu, Q. Wei, G. Liu and J. Ding, *Adv. Sci.*, 2023, **10**, 2206154.
8 Y. Yang, P. K. Qi, Z. L. Yang and N. Huang, *Biosurface Biotribology*, 2015, **1**, 177–201.
9 S. F. Bernatchez, V. Menon, J. Stoffel, S.-A. H. Walters, W. E. Lindroos, M. C. Crossland, L. G. Shawler, S. P. Crossland and J. V. Boykin Jr., *Wound Repair Regeneration*, 2013, **21**, 410–417.
10 P. C. Lee, A. N. Salyapongse, G. A. Bragdon, L. L. Shears 2nd, S. C. Watkins, H. D. Edington and T. R. Billiar, *Am. J. Physiol.*, 1999, **277**, H1600–H1608.
11 T. R. Lizarbe, C. García-Rama, C. Tarín, M. Saura, E. Calvo, J. A. López, C. López-Otín, A. R. Folgueras, S. Lamas and C. Zaragoza, *FASEB J.*, 2008, **22**, 3207–3215.
12 K. Yamasaki, H. D. Edington, C. McClosky, E. Tzeng, A. Lizonova, I. Kovesdi, D. L. Steed and T. R. Billiar, *J. Clin. Invest.*, 1998, **101**, 967–971.
13 M. J. Malone-Povolny, S. E. Maloney and M. H. Schoenfisch, *Adv. Healthcare Mater.*, 2019, **8**, e1801210.
14 M. Wu, Z. Lu, K. Wu, C. Nam, L. Zhang and J. Guo, *J. Mater. Chem. B*, 2021, **9**, 7063–7075.
15 T. P. Amadeu and A. M. A. Costa, *J. Cutaneous Pathol.*, 2006, **33**, 465–473.
16 A. B. Shekhter, V. A. Serezhenkov, T. G. Rudenko, A. V. Pekshev and A. F. Vanin, *Nitric Oxide*, 2005, **12**, 210–219.
17 G. Badr, W. N. Hozzein, B. M. Badr, A. Al Ghamdi, H. M. Saad Eldien and O. Garraud, *J. Cell. Physiol.*, 2016, **231**, 2159–2171.
18 M. A. Shalaby, M. M. Anwar and H. Saeed, *J. Polym. Res.*, 2022, **29**, 91.
19 D. A. Riccio and M. H. Schoenfisch, *Chem. Soc. Rev.*, 2012, **41**, 3731–3741.
20 A. K. Yamala, V. Nadella, Y. Mastai, H. Prakash and P. Paik, *Nanoscale*, 2017, **9**, 14006–14014.
21 J. F. Quinn, M. R. Whittaker and T. P. Davis, *J. Controlled Release*, 2015, **205**, 190–205.
22 J. Cao, M. Su, N. Hasan, J. Lee, D. Kwak, D. Y. Kim, K. Kim, E. H. Lee, J. H. Jung and J.-W. Yoo, *Pharmaceutics*, 2020, **12**, 926.
23 M. Li, J. Aveyard, K. G. Doherty, R. C. Deller, R. L. Williams, K. N. Kolegraff, S. B. Kaye and R. A. D'Sa, *ACS Mater. Au*, 2022, **2**, 190–203.
24 T. H. Bindu, M. Vidyavathi, K. Kavitha, Tp. Sastry and S. Rv, *Int. J. Drug Delivery*, 2010, **2**, 173–182.
25 D. Wei and X. Zhang, *Biosaf. Health*, 2022, **4**, 118–134.
26 Y. Zhang, Y. Xu, H. Kong, J. Zhang, H. F. Chan, J. Wang, D. Shao, Y. Tao and M. Li, *Exploration*, 2023, **3**, 20210170.
27 J. Yang and J. Ding, *BME Front.*, 2023, **4**, 0020.
28 U. Shimanovich, A. Lipovsky, D. Eliaz, S. Zigdon, T. P. J. Knowles, Y. Nitzan, S. Michaeli and A. Gedanken, *Adv. Healthcare Mater.*, 2015, **4**, 723–728.
29 WHO, WHO model list of essential medicines, 20th list (March 2017, amended August 2017), **https://apps.who.int/iris/bitstream/handle/10665/273826/EML-20-eng.pdf**, (accessed 12-05-2023, 2023).
30 R. Ahmed, R. Augustine, M. Chaudhry, U. A. Akhtar, A. A. Zahid, M. Tariq, M. Falahati, I. S. Ahmad and A. Hasan, *Biomed. Pharmacother.*, 2022, **149**, 112707.
31 Y. Kang, J. Kim, Y. M. Lee, S. Im, H. Park and W. J. Kim, *J. Controlled Release*, 2015, **220**, 624–630.
32 A. K. Yamala, V. Nadella, Y. Mastai, H. Prakash and P. Paik, *J. Appl. Polym. Sci.*, 2020, **137**, 48363.
33 I. Greco, N. Molchanova, E. Holmedal, H. Jenssen, B. D. Hummel, J. L. Watts, J. Håkansson, P. R. Hansen and J. Svenson, *Sci. Rep.*, 2020, **10**, 13206.
34 H. Hussain, R. L. Santhana, S. Ahmad, M. F. Abd Razak, W. N. Wan Mohamud, J. Bakar and H. M. Ghazali, *Cogent Food Agric.*, 2019, **5**, 1582398.
35 S. Mukherjee, P. Sriram, A. K. Barui, S. K. Nethi, V. Veeriah, S. Chatterjee, K. I. Suresh and C. R. Patra, *Adv. Healthcare Mater.*, 2015, **4**, 1722–1732.
36 M. M. D. Villiers, in *Ointment bases*, ed. J. E. Thompson, Lippincott Williams & Wilkins, 2009, pp. 277–290.
37 R. Weller, *Clin. Exp. Dermatol.*, 2003, **28**, 511–514.
38 H. Razmi and H. Heidari, *Anal. Biochem.*, 2009, **388**, 15–22.
39 Z. Xun, C. Cai and T. Lu, *Electroanalysis*, 2004, **16**, 674–683.
40 A. Chakraborty, S. Pacelli, S. Alexander, S. Huayamares, Z. Rosenkrans, F. E. Vergel, Y. Wu, A. Chakravorty and A. Paul, *Mol. Pharm.*, 2023, **20**, 767–774.

41 T. Goyal and C. L. Schmotzer, *Am. J. Clin. Pathol.*, 2015, **143**, 579–583.
42 R. Li, K. Liu, X. Huang, D. Li, J. Ding, B. Liu and X. Chen, *Adv. Sci.*, 2022, **9**, 2105152.
43 N. S. Kamal, Y. S. R. Krishnaiah, X. Xu, A. S. Zidan, S. Raney, C. N. Cruz and M. Ashraf, *Int. J. Pharm.*, 2020, **590**, 119914.
44 Y. Zhang, K. Tang, B. Chen, S. Zhou, N. Li, C. Liu, J. Yang, R. Lin, T. Zhang and W. He, *Biomater. Sci.*, 2019, **7**, 1607–1616.
45 R. González, F. J. Molina-Ruiz, J. A. Bárcena, C. A. Padilla and J. Muntané, *Antioxid. Redox Signaling*, 2017, **29**, 1312–1332.
46 P. Deng, L. Yao, J. Chen, Z. Tang and J. Zhou, *Carbohydr. Polym.*, 2022, **276**, 118718.
47 V. C. O. Póvoa, G. J. V. P. dos Santos, G. F. Picheth, C. P. Jara, L. C. E. da Silva, E. P. de Araújo and M. G. de Oliveira, *J. Tissue Eng. Regen. Med.*, 2020, **14**, 807–818.
48 Y. Oh, H. Jeong, S. Lim and J. Hong, *Biomacromolecules*, 2020, **21**, 4972–4979.
49 T. A. Wilgus, *Adv. Wound Care*, 2019, **8**, 671–678.
50 S. C. R. Santos, C. Miguel, I. Domingues, A. Calado, Z. Zhu, Y. Wu and S. Dias, *Exp. Cell Res.*, 2007, **313**, 1561–1574.
51 M. Moreno-Sastre, M. Pastor, A. Esquisabel, E. Sans, M. Viñas, D. Bachiller and J. L. Pedraz, *J. Microencapsulation*, 2016, **33**, 636–645.
52 L. M. Ernst, E. Casals, P. Italiani, D. Boraschi and V. Puntes, *Nanomaterials*, 2021, **11**, 2991.
53 J. Tan, T. J. Cho, D. H. Tsai, J. Liu, J. M. Pettibone, R. You, V. A. Hackley and M. R. Zachariah, *Langmuir*, 2018, **34**, 154–163.
54 C. Thauvin, B. Schwarz, F. Delie and E. Allémann, *Int. J. Pharm.*, 2018, **548**, 771–777.
55 X. Xu, M. Al-Ghabeish, Y. S. R. Krishnaiah, Z. Rahman and M. A. Khan, *Int. J. Pharm.*, 2015, **494**, 31–39.
56 M. R. Holme and T. Sharman, Sodium nitroprusside, **https://www.ncbi.nlm.nih.gov/books/NBK557487/**, (accessed 07-05-2023, 2023).
57 S. Liu, X. Cai, W. Xue, D. Ma and W. Zhang, *Carbohydr. Polym.*, 2020, **234**, 115928.
58 J. Lee, S. P. Hlaing, J. Cao, N. Hasan and J.-W. Yoo, *J. Pharm. Invest.*, 2020, **50**, 505–512.
59 H. T. T. Duong, Z. M. Kamarudin, R. B. Erlich, Y. Li, M. W. Jones, M. Kavallaris, C. Boyer and T. P. Davis, *Chem. Commun.*, 2013, **49**, 4190–4192.
60 M. Huang, J. Zhang, X. Ke, S. Gao, D. Wu, J. Chen and Y. Weng, *RSC Adv.*, 2022, **12**, 2383–2390.
61 S. Ghalei, M. Douglass and H. Handa, *ACS Biomater. Sci. Eng.*, 2022, **8**, 273–283.
62 G. K. Rout, H.-S. Shin, S. Gouda, S. Sahoo, G. Das, L. F. Fraceto and J. K. Patra, *Artif. Cells, Nanomed., Biotechnol.*, 2018, **46**, 1053–1062.
63 J. Lee, D. Kwak, H. Kim, J. Kim, S. P. Hlaing, N. Hasan, J. Cao and J.-W. Yoo, *Pharmaceutics*, 2020, **12**, 618.
64 H. Nurhasni, J. Cao, M. Choi, I. Kim, B. L. Lee, Y. Jung and J. W. Yoo, *Int. J. Nanomed.*, 2015, **10**, 3065–3080.
65 G. Han, L. N. Nguyen, C. Macherla, Y. Chi, J. M. Friedman, J. D. Nosanchuk and L. R. Martinez, *Am. J. Pathol.*, 2012, **180**, 1465–1473.
66 N. Yamamoto, T. Oyaizu, M. Enomoto, M. Horie, M. Yuasa, A. Okawa and K. Yagishita, *Sci. Rep.*, 2020, **10**, 2744.
67 E. Pereverzeva, I. Treschalin, M. Treschalin, D. Arantseva, Y. Ermolenko, N. Kumskova, O. Maksimenko, V. Balabanyan, J. Kreuter and S. Gelperina, *Int. J. Pharm.*, 2019, **554**, 161–178.
68 P. Bao, A. Kodra, M. Tomic-Canic, M. S. Golinko, H. P. Ehrlich and H. Brem, *J. Surg. Res.*, 2009, **153**, 347–358.
69 P. Martin and S. J. Leibovich, *Trends Cell Biol.*, 2005, **15**, 599–607.
70 A. Woodfin, M.-B. Voisin and S. Nourshargh, *Arterioscler., Thromb., Vasc. Biol.*, 2007, **27**, 2514–2523.